Performance of the ALEPH detector at LEP

D. Buskulic, D. Casper, I. de Bonis, D. Decamp, P. Ghez, C. Goy, J.P. Lees, M.N. Minard, P. Odier, B. Pietrzyk, et al.

EUROPEAN ORGANIZATION FOR NUCLEAR RESEARCH

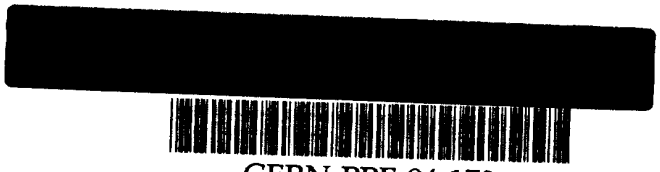

CERN-PPE-94-170

CERN-PPE/94-170
1 November 1994

Performance of the ALEPH detector at LEP

The ALEPH Collaboration*

Abstract

The performance of the ALEPH detector at the LEP e^+e^- collider is reviewed. The accuracy of the tracking detectors to measure the impact parameter and momentum of charged tracks is specified. Calorimeters are used to measure photons and neutral hadrons, and the accuracy obtained in energy and angle is given. An essential property of the detector is its ability to identify particles; the performance in identification of electrons, muons, neutrinos (from missing energy), charged hadrons, π^0's and V^0's is described.

(To be submitted to Nucl. Instr. Meth. A)

*See the following pages for the list of authors.

[1]Now at CERN, 1211 Geneva 23, Switzerland.
[2]Deceased.
[3]Now at Harvard University, Cambridge, MA 02138, U.S.A.
[4]Also Istituto di Fisica Generale, Università di Torino, Torino, Italy.
[5]Also Istituto di Cosmo-Geofisica del C.N.R., Torino, Italy.
[6]Now at Parallax Solutions Limited, Univ. of Warwick Science Park, Coventry, CV4 7EZ, U.K.
[7]Supported by CICYT, Spain.
[8]Supported by the National Science Foundation of China.
[9]Supported by the Danish Natural Science Research Council.
[10]Supported by the UK Science and Engineering Research Council.
[11]Supported by the US Department of Energy, contract DE-AC02-76ER00881.
[12]On leave from Universitat Autonoma de Barcelona, Barcelona, Spain.
[13]Supported by the US Department of Energy, contract DE-FG05-92ER40742.
[14]Supported by the US Department of Energy, contract DE-FC05-85ER250000.
[15]Present address: Lion Valley Vineyards, Cornelius, Oregon, U.S.A.
[16]Supported by the Bundesministerium für Forschung und Technologie, Fed. Rep. of Germany.
[17]Supported by the Direction des Sciences de la Matière, C.E.A.
[18]Supported by Fonds zur Förderung der wissenschaftlichen Forschung, Austria.
[19]Permanent address: Kangnung National University, Kangnung, Korea.
[20]Now at Dipartimento di Fisica, Università di Milano, Milano, Italy.
[21]Also at CERN, PPE Division, 1211 Geneva 23, Switzerland.
[22]Supported by the US Department of Energy, grant DE-FG03-92ER40689.
[23]Now at Università di Pavia, Pavia, Italy.
[24]Now at Rutgers University, Piscataway, NJ 08854, USA.
[25]Now at University of Pittsburgh, Pittsburgh, PA 15260, U.S.A.
[26]Partially supported by Colciencias, Colombia.
[27]Also at Istituto di Matematica e Fisica, Università di Sassari, Sassari, Italy.
[28]Permanent address: Universitat de Barcelona, 08208 Barcelona, Spain.
[29]Now at SLAC, Stanford, CA 94309, U.S.A.
[30]Now at Rheinische Friedrich-Wilhelms-Universität Bonn, 5300 Bonn 1, Germany.
[31]Now at Columbia University, New York NY10027, U.S.A.
[32]Now at Harvard University, Cambridge MA02138, U.S.A.
[33]Now at CALTECH, Pasadena CA 91125, U.S.A.
[34]Now at LBL, Berkeley CA 94720, U.S.A.
[35]Now at SLAC, Stanford CA 94309, U.S.A.
[36]Now at University of Oregon, U.S.A.
[37]Now at SSC Laboratory, Dallas TX 75237, U.S.A.
[38]Now at FNAL, Batavia IL 60510, U.S.A.
[39]Now at DESY, 22603 Hamburg, Germany.
[40]Now at University at Chicago, Chicago IL 60680, U.S.A.
[41]Now at ETH, 5232 Villingen, Switzerland.
[42]Now at Humboldt Universitz, 10115 Berlin, Germany.
[43]Now at Le Croy, 1217 Geneva, Switzerland.
[44]Now at University of Birmingham, Birmingham B15 2TT, U.K.
[45]Now at Johannes-Gutenberg University, 6500 Mainz, Germany.
[46]Now at Max-Planck-Institut für Kernphysik, 6900 Heidelberg, Germany.

D. Abbaneo, C. Avanzini, G. Bagliesi, G. Batignani, A. Bechini, F. Bosi, U. Bottigli, C. Bozzi, C. Bradaschia, G. Calderini, M. Carpinelli, C. Cerri, M.A. Ciocci, V. Ciulli, R. Dell'Orso, R. Fantechi, I. Ferrante, F. Fidecaro, F. Forti, A. Giassi, M.A. Giorgi, A. Gregorio, F. Ligabue, R. Lorenzini, A. Lusiani, P.S. Marrocchesi, A. Messineo, G. Pagani, G. Pierazzini, A. Profeti, G. Rizzo, G. Sanguinetti, P. Spagnolo, J. Steinberger, R. Tenchini,[21] G. Tonelli,[27] G. Triggiani, C. Vannini, P.G. Verdini, J. Walsh

Dipartimento di Fisica dell'Università, INFN Sezione di Pisa, e Scuola Normale Superiore, 56010 Pisa, Italy

A.P. Betteridge, Y. Gao, M.G. Green, B.J. Green, D.L. Johnson, P.V. March, T. Medcalf, Ll.M. Mir, I.S. Quazi, J.A. Strong

Department of Physics, Royal Holloway & Bedford New College, University of London, Surrey TW20 OEX, United Kingdom[10]

V. Bertin, J. Bizzell, D.R. Botterill, R.W. Clifft, T.R. Edgecock, S. Haywood, M. Edwards, P.R. Norton, J.C. Thompson, A.W. Tucker

Particle Physics Dept., Rutherford Appleton Laboratory, Chilton, Didcot, Oxon OX11 OQX, United Kingdom[10]

D. Bederede, R. Bernard, E. Beuville, B. Bloch-Devaux, P. Colas, H. Desportes, H. Duarte, S. Emery, L. Gosset, J. Heitzmann, M. Jacquemet, A. Joudon, W. Kozanecki, E. Lançon, M.C. Lemaire, E. Locci, J.C. Lottin, P. Micolon, J. Pascual, P. Perez, J. Rander, J.-F. Renardy, A. Rosowsky, A. Roussarie, J.-P. Schuller, J. Schwindling, D. Si Mohand, B. Vallage

CEA, DAPNIA/Service de Physique des Particules, CE-Saclay, 91191 Gif-sur-Yvette Cedex, France[17]

R.P. Johnson, A.M. Litke, G. Taylor, J. Wear

Institute for Particle Physics, University of California at Santa Cruz, Santa Cruz, CA 95064, USA[22]

A. Beddall, C.N. Booth, S. Cartwright, F. Combley, I. Dawson, A. Koksal, C. Rankin, L.F. Thompson

Department of Physics, University of Sheffield, Sheffield S3 7RH, United Kingdom[10]

A. Böhrer, S. Brandt, G. Cowan, E. Feigl, G. Gillessen, C. Grupen, G. Lutters, J. Minguet-Rodriguez, F. Rivera,[26] P. Saraiva, U. Schäfer, L. Smolik

Fachbereich Physik, Universität Siegen, 57068 Siegen, Fed. Rep. of Germany[16]

L. Bosisio, R. Della Marina, G. Giannini, B. Gobbo, L. Pitis, F. Ragusa[20]

Dipartimento di Fisica, Università di Trieste e INFN Sezione di Trieste, 34127 Trieste, Italy

J. Rothberg, S. Wasserbaech

Experimental Elementary Particle Physics, University of Washington, WA 98195 Seattle, U.S.A.

L. Bellantoni, A. Caldwell,[31] D. Cinabro,[32] J.S. Conway,[24] D.F. Cowen,[33] Z. Feng, D.P.S. Ferguson, Y.S. Gao, J. Grahl, J.L. Harton, O.J. Hayes, H. Hu, R.C. Jared,[34] D. Muller,[35] J.M. Nachtman, Y.B. Pan, Y. Saadi, M. Schmitt, I. Scott, V. Sharma, D. Strom,[36] M. Takashima,[37] J.D. Turk, A.M. Walsh, F.V. Weber,[1] E. Wicklund,[38] Sau Lan Wu, X. Wu, J.M. Yamartino, M. Zheng, G. Zobernig

Department of Physics, University of Wisconsin, Madison, WI 53706, USA[11]

E. Focardi, G. Parrini, E. Scarlini

Dipartimento di Fisica, Università di Firenze, INFN Sezione di Firenze, 50125 Firenze, Italy

M. Corden, M. Delfino,[12] C. Georgiopoulos, D.E. Jaffe, D. Levinthal[15]

Supercomputer Computations Research Institute, Florida State University, Tallahassee, FL 32306-4052, USA [13,14]

M. Anelli, A. Antonelli, A. Balla, G. Bencivenni, G. Bologna,[4] R. Bonini, F. Bossi, P. Campana, G. Capon, M. Carletti, F. Cerutti, V. Chiarella, G. Corradi, B. Dulach, G. Felici, P. Laurelli, G. Mannocchi,[5] F. Murtas, G.P. Murtas, M. Pepe-Altarelli, P. Picchi, S. Salomone, M. Santoni

Laboratori Nazionali dell'INFN (LNF-INFN), 00044 Frascati, Italy

P. Colrain, I. ten Have, I.G. Knowles, J.G. Lynch, W. Maitland, W.T. Morton, C. Raine, P. Reeves, J.M. Scarr, K. Smith, M.G. Smith, A.S. Thompson, S. Thorn, R.M. Turnbull

Department of Physics and Astronomy, University of Glasgow, Glasgow G12 8QQ,United Kingdom[10]

U. Becker, B. Brandl, O. Braun, R. Geiges,[45] C. Geweniger, P. Hanke, V. Hepp, W. Heyde,[2] E.E. Kluge, J. Krause, Y. Maumary,[1] M. Panter,[46] A. Putzer,[21] B. Rensch, M. Schmidt, K. Schmitt, A. Stahl,[30] H. Stenzel, K. Tittel, M. Wunsch

Institut für Hochenergiephysik, Universität Heidelberg, 69120 Heidelberg, Fed. Rep. of Germany[16]

G.J. Barber, R. Beuselinck, D.M. Binnie, W. Cameron, M. Cattaneo, D.J. Colling, D.N. Gentry, J.F. Hassard, N. Konstantinidis, D.G. Miller, L. Moneta, A. Moutoussi, J. Nash, D.G. Payne, D.R. Price, G. San Martin, J.K. Sedgbeer, A.G. Wright

Department of Physics, Imperial College, London SW7 2BZ, United Kingdom[10]

P. Girtler, D. Kuhn, G. Rudolph, R. Vogl

Institut für Experimentalphysik, Universität Innsbruck, 6020 Innsbruck, Austria[18]

C.K. Bowdery, T.J. Brodbeck, A.J. Finch, F. Foster, G. Hughes, D. Jackson, N.R. Keemer, M. Nuttall, A. Patel, T. Sloan, S.W. Snow, E.P. Whelan

Department of Physics, University of Lancaster, Lancaster LA1 4YB, United Kingdom[10]

L.A.T. Bauerdick,[39] A. Galla, A.M. Greene, K. Kleinknecht, J. Raab, B. Renk, H.-G. Sander, H. Schmidt, S.M. Walther, R. Wanke, B. Wolf

Institut für Physik, Universität Mainz, 55099 Mainz, Fed. Rep. of Germany[16]

A.M. Bencheikh, C. Benchouk, M. Billaut, A. Bonissent, D. Calvet, J. Carr, C. Diaconu, F. Etienne, Y. Gally. D. Nicod, P. Payre, L. Roos, D. Rousseau, P. Schwemling, M. Talby

Centre de Physique des Particules, Faculté des Sciences de Luminy, IN^{2}P^3-CNRS, 13288 Marseille, France

I. Abt, K. Ackermann, S. Adlung, R. Assmann, C. Bauer, H. Becker, W. Blum, D. Brown, P. Cattaneo,[23] B. Dehning, H. Dietl, F. Dydak,[21] H. Fischer, A.W. Halley, D. Hauff, P. Holl, K. Jakobs, W. Kothhuber, H. Kroha, J. Lauber, G. Lütjens, G. Lutz, W. Männer, H.-G. Moser, R. Richter, J. Schröder, A.S. Schwarz, R. Settles, H. Seywerd, H. Stieg, U. Stiegler, U. Stierlin,[2] R. St. Denis, L. Strüder, G. Waltermann, P. Weissbach, G. Wolf

Max-Planck-Institut für Physik, Werner-Heisenberg-Institut, 80805 München, Fed. Rep. of Germany[16]

J.-N. Albert, R. Alemany, C. Arnault, R. Bernier, J. Boucrot, O. Callot, R. Chase, A. Cordier, M. Davier, M. Dialinas, A. Ducorps, L. Duflot, J.-F. Grivaz, Ph. Heusse, P. Janot, Ph. Jean, D.W. Kim,[19] F. Le Diberder, J. Lefrançois, A.-M. Lutz, G. Musolino, H.J. Park, J.-P. Richer, M.-H. Schune, J.-J.Veillet, I. Videau

Laboratoire de l'Accélérateur Linéaire, Université de Paris-Sud, IN^{2}P^3-CNRS, 91405 Orsay Cedex, France

The ALEPH Collaboration

D. Buskulic, D. Casper, I. De Bonis, D. Decamp, P. Ghez, C. Goy, J.-P. Lees, M.-N. Minard, P. Odier, B. Pietrzyk

Laboratoire de Physique des Particules (LAPP), IN^{2}P^3-CNRS, 74019 Annecy-le-Vieux Cedex, France

F. Ariztizabal, M. Chmeissani, J.M. Crespo, I. Efthymiopoulos, E. Fernandez, M. Fernandez-Bosman, V. Gaitan, Ll. Garrido,[28] M. Martinez, T. Mattison,[29] S. Orteu, A. Pacheco, C. Padilla, F. Palla, A. Pascual, J.A. Perlas, F. Sanchez F. Teubert,

Institut de Fisica d'Altes Energies, Universitat Autonoma de Barcelona, 08193 Bellaterra (Barcelona), Spain[7]

F. Chiumarulo, A. Clemente, D. Creanza, M. de Palma, A. Farilla, R. Ferorelli, G. Iaselli, G. Maggi, N. Marinelli, A. Mastrogiacomo, S. Natali, V. Negro, S. Nuzzo, M. Papagni, C. Pinto, A. Ranieri, G. Raso, F. Romano, F. Ruggieri, G. Selvaggi, L. Silvestris, P. Tempesta, G. Zito

Dipartimento di Fisica, INFN Sezione di Bari, 70126 Bari, Italy

Y. Chai, D. Huang, X. Huang, J. Lin, T. Wang, Y. Xie, D. Xu, R. Xu, J. Zhang, L. Zhang, W. Zhao

Institute of High-Energy Physics, Academia Sinica, Beijing, The People's Republic of China[8]

H. Albrecht,[39] A. Ball, R. Benetta, F. Bird,[37] E. Blucher,[40] G. Bonvicini, J. Boudreau,[25] T. Charity, P. Comas, P. Coyle, H. Drevermann, A. Engelhardt, M. Ferro-Luzzi, L. Foà, R.W. Forty, M. Frank, G. Ganis, C. Gay,[3] R. Geiges, M. Girone, C. Graab,[41] R. Grabit, J. Griffith, R. Grub, R. Hagelberg, J. Harvey, B. Ivesdal, R. Jacobsen, P. Jarron, B. Jost, M. Kasemann,[39] G. Kellner, J. Knobloch, A. Lacourt, P. Lazeyras, I. Lehraus, B. Lofstedt, T. Lohse,[42] D. Lütze,[39] M. Maggi, A. Marchioro, C. Markou, E.B. Martin, P. Mato, J.-M. Maugain, J. May, H. Meinhard, V. Mertens,[1] A. Minten, A. Miotto, R. Miquel, P. Palazzi, J.R. Pater, P. Perrodo, R. Pintus, L. Pregernig, M. Price, J.-F. Pusztaszeri, F. Ranjard, J. Richstein,[43] W. Richter, L. Rolandi, H. Rotscheidt, W. von Ruden, M. Saich,[6] J.-C. Santiard, P. Schilly, D. Schlatter, M. Schmelling, G. Stefanini, H. Taureg, W. Tejessy, I.R. Tomalin, R. Veenhof, A. Venturi, H. Verweij, H. Wachsmuth, H. Wahl, S. Wheeler,[44] W. Wiedenmann, T. Wildish, W. Witzeling, J. Wotschack

European Laboratory for Particle Physics (CERN), 1211 Geneva 23, Switzerland

Z. Ajaltouni, M. Bardadin-Otwinowska, A. Barres, C. Boyer, M. Brossard, R. Chadelas, F. Daudon, A. Falvard, P. Gay, C. Guicheney, P. Henrard, J. Jousset, B. Michel, J-C. Montret, D. Pallin, P. Perret, F. Podlyski, J. Proriol, F. Saadi

Laboratoire de Physique Corpusculaire, Université Blaise Pascal, IN^{2}P^3-CNRS, Clermont-Ferrand, 63177 Aubière, France

H. Bertelsen, T. Fearnley, F. Hansen, J.B. Hansen, J.D. Hansen, J.R. Hansen, P.H. Hansen, S.D. Johnson, A. Lindahl, B. Madsen, R. Møllerud, B.S. Nilsson, G. Petersen

Niels Bohr Institute, 2100 Copenhagen, Denmark[9]

A. Kyriakis, E. Simopoulou, I. Siotis, A. Vayaki, K. Zachariadou

Nuclear Research Center Demokritos (NRCD), Athens, Greece

M. Bercher, U. Berthon, A. Blondel, G. Bonneaud, J.C. Brient, P. Bourdon, A. Busata, M. Cerutti, J. Doublet, G. Fouque, C. Lemoine, P. Matricon, M. Maubras, R. Morano, J.-Y. Parey, L. Passalacqua, P. Poilleux, A. Rougé, C. Roy, M. Rumpf, R. Tanaka, A. Valassi, M. Verderi, H. Videau, C. Violet

Laboratoire de Physique Nucléaire et des Hautes Energies, Ecole Polytechnique, IN^{2}P^3-CNRS, 91128 Palaiseau Cedex, France

D.J. Candlin, A.J. Main, M.I. Parsons, E. Veitch

Department of Physics, University of Edinburgh, Edinburgh EH9 3JZ, United Kingdom[10]

1 Introduction

ALEPH is one of the four detectors at the LEP collider of CERN. It has been in operation for the past five years in the study of e^+e^- collisions at the Z resonance, and is expected to continue in service through the exploitation of LEP at double this energy for at least another such period. The detector has been described elsewhere [1]; here a summary of the performance underlying the data analysis is presented.

ALEPH is a particle detector, covering as much of the 4π solid angle as possible (see Figure 1). It is designed to measure the momenta of charged particles, to measure the energy deposited in calorimeters by charged and neutral particles, to identify the three lepton flavours, and to measure the distance of travel of short-lived particles such as the tau lepton and the b and c hadrons. Particular emphasis has been given to momentum resolution up to the highest energies (by means of a large tracking system in a 1.5 T magnetic field), to electron identification (by means of a highly segmented, projective electromagnetic calorimeter, as well as ionization measurement in the tracking system), and to muon identification (with continuous tracking inside sufficient iron absorber to eliminate the hadrons).

The tracking system involves three detectors: a vertex detector composed of two layers of double-sided silicon microstrips, a drift chamber with 30 cm outer radius, which is also important as part of the trigger system, and a time projection chamber (TPC) with 180 cm outer radius. Calorimetry proceeds in two stages, electromagnetic and hadronic.

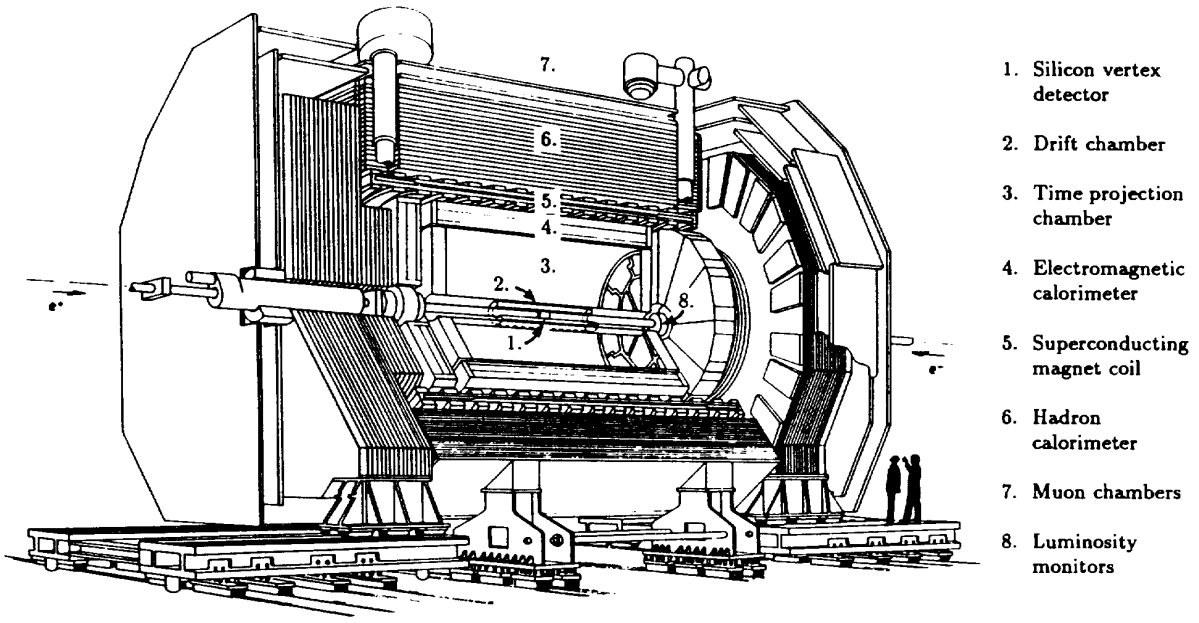

Figure 1: Perspective view of the ALEPH detector.

The electromagnetic calorimeter is a 45 layer lead/proportional-chamber sandwich, and the hadron calorimeter is a 23 layer iron/streamer-tube sandwich with total thickness of 120 cm of iron (the magnet return yoke). The whole is surrounded by an additional muon detection system of two double-layers of streamer tubes. Finally, important for precise cross-section measurement is the highly segmented luminosity calorimeter, composed of twelve-layer tungsten/silicon sandwiches that surround the beam pipe at each end.

The presentation is divided as follows: in the next section, the performance of the trigger of the apparatus is described. Then in Section 3 the tracking performance is discussed, including spatial and momentum resolution. This is followed by a description of the specific ionization (dE/dx) measurement from the TPC in Section 4, and the calorimeter performance in Section 5. The subsequent sections describe particle identification, for respectively electrons, muons, photons and neutral pions, and V^0's. These features of the detector are applied in Section 10 to the global description of events, using energy flow, and finally the measurement of luminosity is covered in Section 11.

2 Trigger performance

Understanding the efficiency of the trigger is crucial in many of the analyses at LEP which demand precise measurements of cross-sections. The ALEPH trigger system is based on the use of four approaches to derive trigger signals:

1. Energy deposits in the electromagnetic calorimeter (Total-energy trigger), demanding ~ 6 GeV in the barrel, ~ 3 GeV in either end-cap, or ~ 1.5 GeV in both end-caps.

2. Track segments in the drift chamber in coincidence with an energy deposit in the module of the electromagnetic calorimeter to which the track is pointing (Electron-track trigger). The threshold is set to 200 MeV, which corresponds to less than 50 % of the energy deposit of a muon in the electromagnetic calorimeter.

3. Track segments in the drift chamber in coincidence with hits in a module of the hadron calorimeter, so requiring a certain penetration depth (Muon-track trigger). This trigger is sensitive to muons and, with lower efficiency, to hadrons.

4. Two track segments back-to-back in the drift chamber (Back-to-back trigger).

The system relies on multiple triggers being delivered for each physics channel. The simplicity of the trigger logic and the redundancy allows trigger efficiencies near 100 % to be obtained as well as providing cross-checks for verifying the efficiency of the individual triggers.

Hadronic Z decays are collected using two main triggers, the Total-energy and Muon-track triggers. The combination of these triggers has an efficiency of greater than 99.99 % for hadronic Z decays, with an uncertainty of less than 0.01 %, which has been determined by comparing the rates for one or both of the triggers firing.

Leptonic events have a lower multiplicity than hadronic events, and so require larger redundancy. For muons three triggers are used: the Muon-track, Electron-track, and Back-to-back triggers. The combined efficiency of these triggers is very near to 100 %; the first is measured to be larger than 99.8 % and all three of these triggers are present in more than 98 % of muon pair events. The same triggers are used to select tau events, again achieving close to 100 % efficiency. Bhabha events, however, which deposit all their energy in the electromagnetic calorimeter, are triggered by the Total-energy trigger with 100 % efficiency. For each of the lepton triggers the efficiencies quoted above are for events in the angular range $|\cos\theta| < 0.9$. The knowledge of the uncertainty on the trigger inefficiency for the leptonic events is limited by statistics to 0.05 %.

In order to study the process $e^+e^- \to \nu\bar{\nu}\gamma$ it is necessary to trigger on a single photon with energy $\sim$ 1–2 GeV. The trigger for these events demands a deposit of at least 1 GeV in a single module of the electromagnetic calorimeter. The efficiency of this trigger approaches 100 % at 1.5 GeV, with an uncertainty of 0.2 %.

The luminosity is measured using Bhabha events in the luminosity calorimeter. The trigger for these events depends on the total energy deposited in the calorimeter. Triggers are constructed using single-arm high threshold triggers, and double-arm low threshold triggers. The efficiencies of these triggers are cross-checked against each other, and against similar downscaled triggers with lower energy thresholds. The overall trigger efficiency is 100 % with an uncertainty of 0.01 %.

The trigger rate is typically 4–5 Hz, where Bhabha events in the luminosity calorimeter contribute 2–3 Hz, Z events (at the peak) and two-photon events contribute about 0.5 Hz each, and the remainder is accounted for by cosmic rays, noise and beam related background.

3 Tracking performance

3.1 Silicon vertex detector

Close to the interaction point, tracking is performed by a silicon vertex detector. This device is formed from 96 silicon wafers each of dimensions $(5.12 \times 5.12 \times 0.03)$ cm, arranged in two coaxial cylinders around the beam pipe. The inner layer has nine wafers in azimuth, with average radius of 6.5 cm, and the outer layer has 15 wafers with average radius 11.3 cm, both layers being four wafers long. Each wafer has 100 μm strip readout both parallel ($r\phi$) and perpendicular (rz) to the beam direction.[†] A detailed description of the vertex detector is given in Reference [2].

Vertex detector hits are used to provide additional precision for tracks already reconstructed in the outer tracking. Hits are reconstructed by averaging the charge-weighted positions of adjacent strips that have at least three times the mean noise charge; they are

[†]The coordinate system used is cylindrical, with radius r, azimuthal angle ϕ and axial coordinate z.

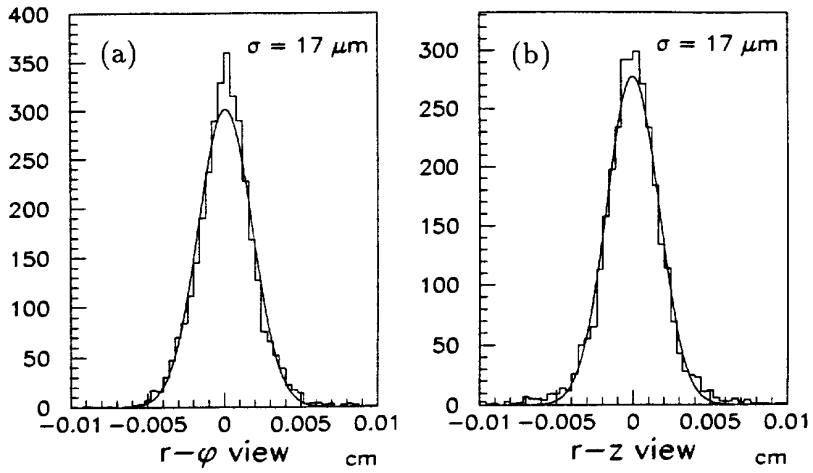

Figure 2: The vertex detector hit separation for tracks passing through overlapping wafers in (a) the $r\phi$ view and (b) the rz view.

associated to tracks by minimizing the χ^2 of a track refit including candidate vertex detector hits. The correlation between the charge measured in the two views is used to identify double-track clusters. Monte Carlo studies show that the vertex detector hit association is correct for 98 % (90 %) of the hadronic Z decay tracks with hits in both (one) layers.

The relative positions of the silicon wafers are determined from the data with no reference to the outer tracking. Tracks which pass through the $\sim$ 5 % active overlap-area between wafers adjacent in ϕ constrain their relative position. Linking the wafers around the full azimuth via their overlap constrains their average radii. Tracks from $Z \rightarrow \mu^+\mu^-$ events constrain the relative position of wafers in different layers and on opposite sides of the detector. The resulting alignment contributes negligibly to the hit errors. Figure 2 shows the measured distance between hits in overlapping wafers for near-normal incident high-momentum ($p > 2\,\mathrm{GeV}/c$) tracks after alignment. Dividing the widths of these distributions by $\sqrt{2}$ gives an effective point resolution of 12 μm in both views. This value is taken as the vertex detector hit resolution in the track fit.

3.2 Drift chamber

The vertex detector is surrounded by a conventional cylindrical drift chamber [1, 3]. It measures the $r\phi$ position of a track on eight concentric layers of hexagonal drift cells at radii between 16 and 26 cm, with adjacent layers staggered by half a cell width. The resolution depends on the drift length in the cell, with an average of 150 μm. The position of tracks along the beam direction is also determined by measuring the difference in arrival time of the signals at each end of the wires. This has a resolution of a few cm and is not used in the standard tracking, but allows the implementation of a three-dimensional first-level track trigger [3].

The position of the drift chamber relative to the TPC is determined with data. Initial

values of the alignment constants are determined with the help of cosmic ray tracks and survey data. The three translational alignment parameters and the three Euler angles relative to the TPC are then measured with tracks from the processes $Z \to \mu^+\mu^-$ and $Z \to q\bar{q}$, by minimizing the residuals between the measured hits and the expected hit positions of tracks extrapolated from the TPC into the drift chamber.

3.3 Time projection chamber

The TPC [1, 4] provides 21 three-dimensional space-point measurements for fully contained tracks at radii between 30 and 180 cm. The ionization charge is recorded at two end-plates by a system of proportional wire chambers (known as sectors), read out using segmented cathode pads arranged in 21 concentric circles.

The relative alignment of the 18 sectors on each end-plate is determined with two-track events from the process $Z \to \mu^+\mu^-$, where the radially outgoing muons have their momentum constrained to the beam energy in the fit. The positions of each sector in the $r\phi$ and rz planes are determined by minimizing the azimuthal and longitudinal deviations between track segments fitted in the individual sectors and track segments fitted in the inner tracking detectors.

The quality of the track reconstruction in the TPC depends critically on precise knowledge of systematic distortions of the tracks during the drift of their ionization towards the end-plates. Distortions due to inhomogeneities of the magnetic and electric fields are determined from a magnetic field map, as measured in 1987 [1], and from the straightness of reconstructed laser tracks in the TPC. A detailed description of the methods to calibrate drift-field distortions with the laser system can be found in Reference [4].

For the measurement of z coordinates one needs to know the drift velocity of electrons in the TPC gas and the time difference between the beam crossing and the start of digitization. This time difference is constant, so the drift velocity can be set by requiring that the tracks from hadronic Z events in the two halves of the TPC come from the same origin. The drift velocity change is determined and updated on a run-by-run basis in a precursor to the full event reconstruction. The method is regularly monitored by comparing the track polar angle reconstructed in the TPC to that observed in the vertex detector, and also by comparing measurements from the laser system.

After all corrections an overall azimuthal coordinate resolution of $\sigma_{r\phi} = 173\,\mu$m [4] is measured with leptonic Z decays for isolated coordinates. The longitudinal resolution is $\sigma_z = 740\,\mu$m for tracks with polar angles within 10° of perpendicular to the beams. The resolution depends on the drift length and the orientation of the track relative to pads and wires. The measured dependence of the resolution has been parametrized and is used to calculate the coordinate errors in the track fit.

3.4 Track reconstruction

Tracks are reconstructed starting in the TPC. Nearby hits are linked to form track segments, and the segments are connected to make tracks by requiring consistency with a helix hypoth-

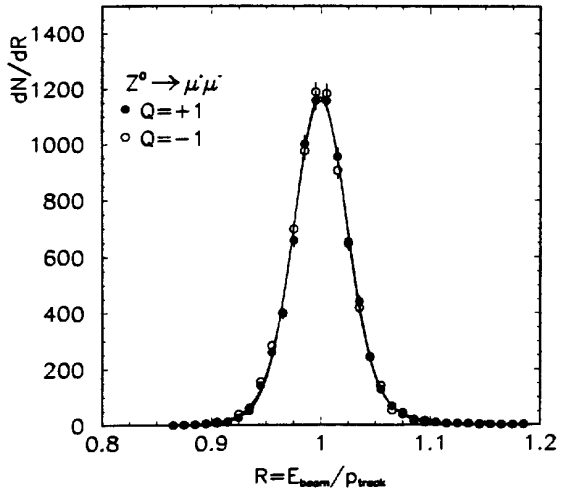

Figure 3: The ratio of the beam energy to the track momentum measured in the tracking system for muons (charge Q) from $Z \rightarrow \mu^+\mu^-$ decays.

esis. These track candidates are extrapolated to the inner detectors where consistent hits are assigned. Coordinate errors are determined using the preliminary track parameters. The final track fit based on Kalman filter [5] techniques uses these errors and takes into account multiple scattering between each measurement. The track finding efficiency in the TPC has been studied using Monte Carlo simulation. In hadronic Z events, 98.6 % of tracks that cross at least four pad rows in the TPC are reconstructed successfully; the small inefficiency, due to track overlaps and cracks, is reproduced to better than 10^{-3} by the simulation. The efficiency of associating a vertex detector hit to an isolated track is about 94 % per layer, within the geometrical acceptance.

The performance of the track reconstruction is studied using $Z \rightarrow \mu^+\mu^-$ decays. Figure 3 shows the ratio of the beam energy to the measured momentum for tracks from dimuon events. Here a track is required to have at least 19 TPC hits, at least six drift chamber hits and at least one vertex detector hit in the $r\phi$ plane. The acollinearity angle between the positive and the negative muon is required to be smaller than 0.2° in order to eliminate radiative events. These events are also removed by requiring the sum of the energies of all clusters in the electromagnetic calorimeter which are not associated with the two muons to be less than 100 MeV. A transverse momentum resolution of

$$\sigma(1/p_T) = 0.6 \times 10^{-3}\ (\mathrm{GeV}/c)^{-1} \qquad (1)$$

is measured (for 45 GeV muons). Table 1 summarizes the measured resolution for TPC only, for TPC and drift chamber, and for all three tracking detectors together. At low momentum multiple scattering dominates and adds a constant term of 0.005 to $\sigma(p_T)/p_T$.

The impact parameter resolution for high momentum charged particles is measured from the distance between the two tracks from dimuon events at the interaction point. The distances projected into the $r\phi$ and rz planes are shown in Figures 4 (a) and (b) for tracks with vertex detector hits in both layers. The width of these distributions is $\sqrt{2}$ times the

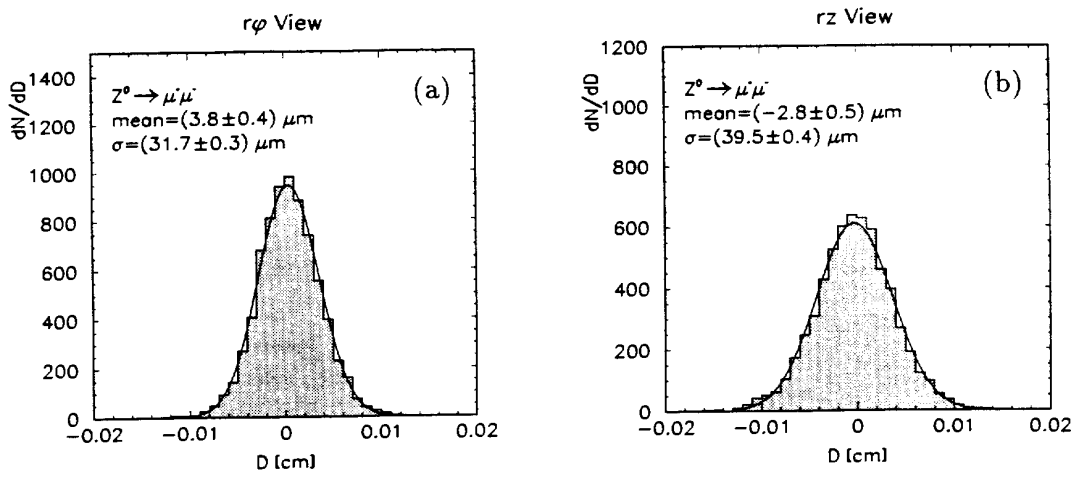

Figure 4: Performance of the track reconstruction: (a) signed distance of closest approach in the $r\phi$ plane, (b) miss-distance perpendicular to the track direction in the rz plane, for $Z \to \mu^+\mu^-$ decays.

impact parameter resolution in the respective direction. From a Gaussian fit one obtains an impact parameter resolution of $23\,\mu$m in the $r\phi$ view and $28\,\mu$m in the rz view for tracks measured in all three tracking detectors. Table 1 summarizes the impact parameter results for high momentum tracks when detectors are successively included in the fit.

The impact parameter resolution of lower momentum charged particles is measured in hadronic Z decays. The impact parameter δ is measured relative to an event-by-event reconstructed Z decay vertex [6]. The resolution is defined as the r.m.s. of a Gaussian fit to the impact parameter distribution for tracks with no apparent lifetime (i.e. for tracks which cross the thrust axis behind the primary vertex), subtracting the estimated vertex resolution in quadrature. Figure 5 shows the impact parameter resolution for tracks with vertex detector hits in both layers, as a function of momentum, separated into the $r\phi$ and rz views. The resolution can be parametrized as

$$\sigma(\delta) = 25\,\mu\text{m} + \frac{95\,\mu\text{m}}{p\,(\text{GeV}/c)^{-1}}\ , \tag{2}$$

Table 1: Momentum and impact parameter resolution; the successive rows show the effect of including the detectors indicated in the fit.

	Transverse momentum	Impact parameter	
Detector	$\sigma(1/p_T)\ (\text{GeV}/c)^{-1}$	$r\phi\ (\mu\text{m})$	$rz\ (\mu\text{m})$
TPC	1.2×10^{-3}	310	808
+ drift chamber	0.8×10^{-3}	107	808
+ vertex detector	0.6×10^{-3}	23	28

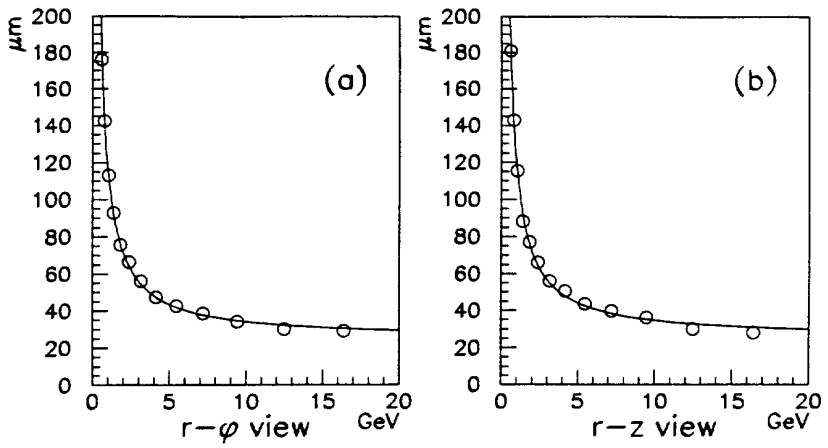

Figure 5: The impact parameter resolution for tracks with vertex detector hits in two layers as a function of their momentum in (a) the $r\phi$ view and (b) the rz view.

in both the $r\phi$ and rz views.

An important use of the precision impact parameter measurement is to detect b hadrons through their lifetime. Figure 6 shows the efficiency versus the purity for tagging a hadronic Z decay event as containing a b hadron, using one or both hemispheres. The b tag algorithm uses the three-dimensional impact parameters of tracks with vertex detector hits to detect the effects of the b lifetime, and is described in Reference [6]. The b tag efficiency is given by the correlation between the tag rates in the two hemispheres of each event, whilst the purity uses Monte Carlo simulation to predict the charm background. The maximum efficiency of 76 % comes from the limited vertex detector solid angle coverage.

The angular and momentum resolution of the tracking system both contribute to the

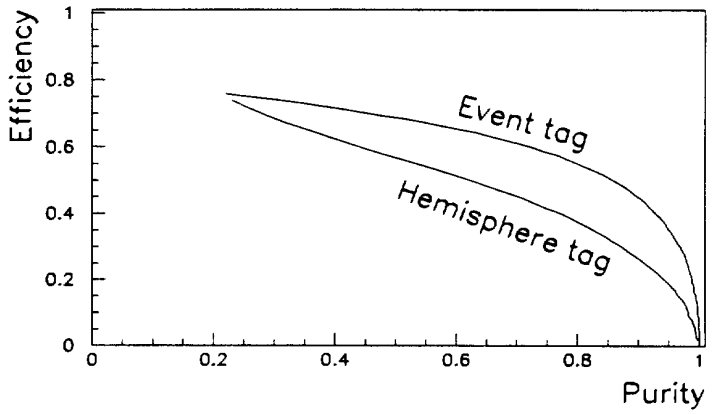

Figure 6: Performance of vertex reconstruction: the efficiency versus purity for tagging a hadronic Z decay event as containing a b hadron, using one or both hemispheres.

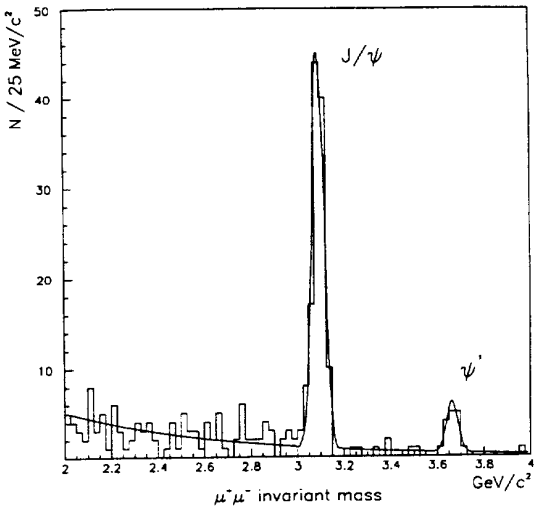

Figure 7: Invariant mass of $\mu^+\mu^-$ pairs, showing a peak at the J/ψ mass (and also at the ψ' mass). The superimposed fit is of a Gaussian for the peaks with an exponential background.

resolution that is achieved on the invariant mass of states that decay into charged particles. This is illustrated in Figure 7, where the $\mu^+\mu^-$ invariant mass is shown, with a clear peak seen for the J/ψ; the resolution on the mass is $25\,\mathrm{MeV}/c^2$.

4 dE/dx measurement

In addition to its role as a tracking device, the TPC also serves to separate particle species according to measurements of their specific energy loss by ionization, dE/dx. The data from the TPC sense wires are used for the dE/dx measurement. The design of the wire chambers, and the almost negligible attenuation of ionization in the drift volume (about 1.3 % per metre), result in a variation in gain over the volume of the TPC of less than 3 % r.m.s. [1]. The ionization from each charged particle is sampled with a sense-wire spacing of 4 mm, giving a total of 338 possible measurements for tracks which traverse the TPC. The dE/dx measurement is important for the identification of electrons and also provides a useful ability to distinguish between pions, kaons and protons in the relativistic rise region.

In the TPC data reduction, tracks are first found using the data from the cathode pads. Wire hits are then associated with track helices by using a simple window in drift time around the projected helix position. Individual wire pulses which match more than a single track are ignored, as are pulses which do not have a shape consistent with ionization from a single track. To avoid bias arising from the non-negligible threshold used in the online zero-suppression algorithm, if a track projects onto a wire which is not known to be dead but nonetheless has no data matching the drift time of the track, then a pulse with a nominal almost-zero ADC value is added to the list of wire pulses. For minimum ionizing particles, an average of 8% of the wire pulses are below threshold and must be treated in this manner.

To minimize sensitivity to the nominal ADC value assigned to such pulses, for each track the wire hits are ordered by pulse height and the hits comprising the lowest 8 % are not included when calculating the mean dE/dx. In addition, the fluctuations due to the long Landau tail are suppressed in the usual way by omitting the highest 40 % of the hits from the mean dE/dx. Thus the dE/dx estimator used is a two-sided truncated mean. The truncation of the lowest 8 % worsens the resolution but is necessary in order to obtain a dE/dx estimator that is independent of the track angle and drift length.[‡]

Variations in track angle result in changes of the sampling length by up to a factor of three in the TPC. Larger sampling lengths give higher ionization statistics per sample and therefore a reduced Landau tail in the pulse-height distribution. The net result is a logarithmic decrease of the truncated mean with increasing sampling length of the form

$$\frac{dE}{dx} \propto \frac{1}{1 + C \ln(\Delta x/\Delta r)} , \tag{3}$$

where $\Delta r = 0.4\,\mathrm{cm}$ is the distance between sense wires and Δx is the corresponding length along the track. The value of C that is used to correct the data is 0.25. Note that this is a purely statistical effect which depends only on the skewed shape of the pulse-height distribution.

Since the TPC operates at atmospheric pressure, the effective gain changes from run to run, with a measured pressure dependence of $\mathcal{P}^{-3.7}$. It is calibrated directly from data using minimum-ionizing pions in the momentum range from $0.3\,\mathrm{GeV}/c$ to $0.6\,\mathrm{GeV}/c$, where there is a large separation between the dE/dx of pions and that of the other particle types. The gain is arbitrarily normalized such that minimum-ionizing particles have $\langle dE/dx \rangle \equiv 1$.

The dE/dx resolution is assumed to be of the form

$$\sigma_I/I = \sigma_0 N^{p_1} (\Delta x/\Delta r)^{p_2} (I/I_0)^{p_3} , \tag{4}$$

where N is the number of wire hits, I is the measured dE/dx and $I_0 \equiv 1$ is the dE/dx at minimum ionization. Data from tracks in hadronic events yield a value of 1.19 for σ_0, while the exponents are measured to be $p_1 = -0.5$ and $p_2 = p_3 \approx -0.4$. This gives a best-case resolution of 4.5 % for an electron with the full complement of wires at a polar angle of $\theta = 45°$. The resolution observed for isolated electrons and muons is consistent with this parametrization derived from measurements of tracks in hadronic jets.

The dependence of the mean dE/dx on particle velocity is measured from data using a variety of event types. Minimum-ionizing pions fix the minimum of the curve, protons are used to fit the low momentum $1/\beta^2$ region, Bhabha events give the plateau position, and dimuons and muons from tau decay give points only slightly below the plateau. The mean dE/dx of pions in the relativistic rise region is determined from fits to dE/dx measurements in hadronic events and is checked using pions from tau decay. In hadronic events, each momentum bin is fitted to a sum of four Gaussian contributions, for electrons, pions, kaons and protons, with only the position of the pion peak and the normalizations of the four contributions allowed to vary. The results of the fits for the position of the pion peak are

[‡]This algorithm has improved substantially since our previous publication of the TPC performance [4].

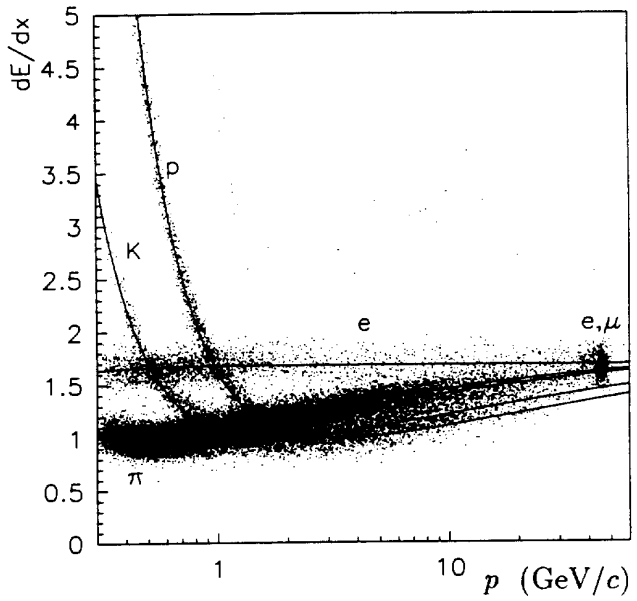

Figure 8: The measured dE/dx versus particle momentum for a sample of about 40,000 tracks. Each track was required to have at least 150 dE/dx measurements. The fitted parametrization is superimposed for electrons, muons, pions, kaons, and protons.

then combined with the points from protons, minimum-ionizing pions, and dileptons in a fit of a modified Bethe-Bloch formula with six free parameters. This procedure is iterated several times, the improved parametrization being used in each iteration to fix the positions of the kaon and proton contributions in the relativistic rise region. The resulting parametrization is plotted over a sample of the data in Figure 8. The 'relativistic rise', the height of the plateau relative to minimum ionization, is found to be 1.66.

Since the objective is to identify particles, the important number is neither the resolution nor the relativistic rise but rather the typical separation, in standard deviations, between particle species in hadronic events. This is heavily influenced by track overlap. Unlike cathode-pad data, wire pulses on a given wire within a single sector are separated only in z, the drift direction. As a result, tracks must be at least 3 cm apart in z in order to be resolved for dE/dx purposes. Considering only the 88 % of tracks in hadronic Z decays with at least 50 dE/dx samples, each gets on average only about 60 % of the maximum possible number of samples. For these tracks, the *average* separation between electrons and pions, pions and kaons, and kaons and protons has been calculated using the parametrizations of the resolution and velocity dependence discussed above and is shown as a function of momentum in Figure 9. Evidently the dE/dx is a powerful tool for electron identification, with greater than 3σ separation up to $p \approx 8\,\mathrm{GeV}/c$. In the relativistic rise region, which is the region of most interest to the experiment, the π-K separation is roughly constant at about 2σ, while the K-p separation is about 1σ. Therefore, kaon and proton identification can be accomplished only on a statistical basis but, nonetheless, is an important means of reducing combinatorial background in many analyses. In the clean environment of one-prong τ decays the particle identification performance is enhanced, reaching 3σ π-K separation [7].

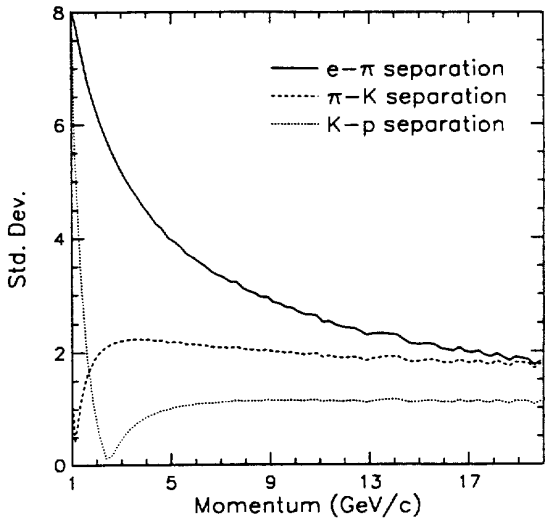

Figure 9: The average dE/dx separation in standard deviations between particle types, computed using all tracks in hadronic Z decays which have at least 50 dE/dx measurements.

5 Calorimeter performance

The first part of this section is devoted to the electromagnetic calorimeter performance concerning its energy and spatial resolution for electromagnetic objects, as well as the uniformity of its response; the second part is devoted to the hadron calorimeter. The performance for hadronic showers, using both calorimeters in an energy-flow algorithm, is discussed in Section 10.

5.1 Electromagnetic calorimeter

The electromagnetic calorimeter is formed of a barrel surrounding the TPC, closed at each end by an end-cap. These are each divided into 12 modules, each covering an azimuthal angle of 30°. The modules have 45 lead/wire-chamber layers, with a total thickness of 22 radiation lengths. The energy and position of each shower is read out using small cathode pads with dimensions $\sim (30 \times 30)$ mm, arranged to form towers pointing to the interaction point; each tower is read out in three segments in depth, known as storeys, corresponding respectively to $(4, 9, 9)$ radiation lengths. There are 74,000 such towers, corresponding to an average granularity of $0.9° \times 0.9°$; this fine segmentation is important in the identification of photons, electrons and neutral pions. In addition, signals are also available from the wire planes of each module, providing redundancy in the energy measurement and a low-noise trigger.

For each module the gas gain is monitored by a small single-wire proportional chamber associated to an Fe^{55} source. The peak of the Fe^{55} source is used to monitor the gain; the

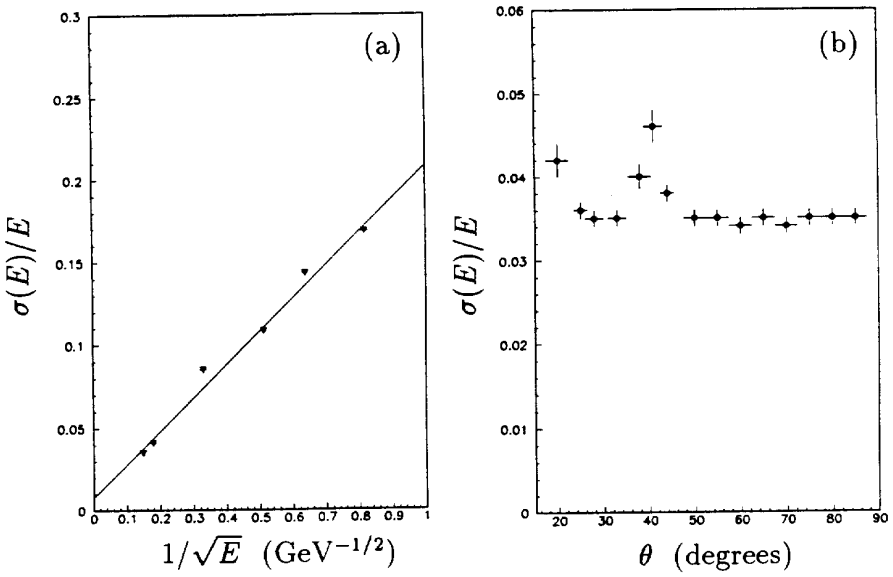

Figure 10: Energy resolution of the electromagnetic calorimeter; (a) dependence on energy, (b) dependence on polar angle for electrons from $Z \to e^+e^-$ decays.

amplitude of the gain variation is limited to 2–3 % over a year as the gas is in a closed-circuit system providing a nearly constant pressure. After correcting for the measured gain variation a stability of better than 0.3 % is reached.

The energy calibration procedure uses electrons from different sources covering the energy range from 1 to 45 GeV. These electrons originate from the reactions $e^+e^- \to e^+e^-e^+e^-$ for the 1 to 10 GeV energy range, $Z \to \tau^+\tau^-$ ($\tau \to e\nu\overline{\nu}$) to cover the 10 to 30 GeV energy range, and Bhabha events for 45 GeV. The basic information used is the output of an algorithm that gathers in a single object, or 'cluster', all individual storeys above a 30 MeV threshold that have in common at least a storey edge or corner. The recorded energy is corrected for energy losses due to the storey threshold, the ionization losses for charged particles before entering the calorimeter, and the leakage of electromagnetic showers not fully contained in the 22 radiation lengths. In addition the non-linearity of the calorimeter response to electrons is corrected using test-beam results, $E_{corr} = E \times (1 + 0.00078E/\mathrm{GeV})$. After accounting for these effects the precision on the module intercalibration is better than 0.3 % at 45 GeV and 1.5 % at lower energy.

The energy resolution, determined by comparing the measured energy to the track momentum or beam energy, is shown in Figure 10 (a) as a function of the electron energy. The corresponding fitted resolution is

$$\frac{\sigma(E)}{E} = \frac{0.18}{\sqrt{E/\mathrm{GeV}}} + 0.009 \ , \tag{5}$$

where a linear sum is used as it gives the best fit; using a quadratic form would give $\sigma(E)/E = 0.178/\sqrt{E/\mathrm{GeV}} \oplus 0.019$. For electrons from Bhabha events the energy resolution is plotted in Figure 10 (b) as a function of polar angle, and shows the degradation of

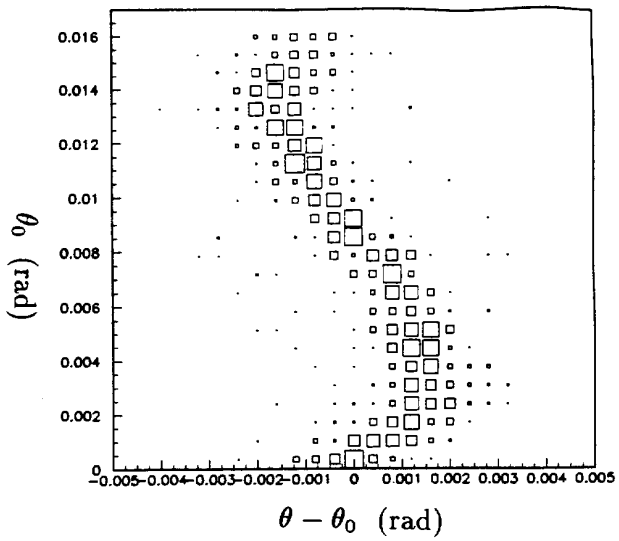

Figure 11: Barycentre reconstruction in the θ angle as a function of the hit coordinate θ_0, determined by extrapolating Bhabha tracks into the calorimeter.

the resolution in two regions of the detector: at small polar angle the fraction of events close to the edge of a module is greater, and the resolution is slightly degraded; the region around 40° in polar angle is the overlap region, where the electromagnetic shower develops into both barrel and end-cap modules. In that region the total thickness decreases, reaching only 16 radiation lengths, and in addition there is more uninstrumented material due to end-plates of modules and cables. To compensate for these energy losses, special corrections are made to showers in that region, evaluated from test-beam results in a comparable set-up. After correction the energy resolution is degraded by about 30 % in the overlap region.

The polar and azimuthal angles of a shower are calculated by an energy-weighted mean of the polar and azimuthal angle of individual storeys in the cluster. The deviation from the expected value obtained using the extrapolation of electron tracks in Bhabha events is shown in Figure 11. The observed 'S-shape' effect is due to the calorimeter granularity being comparable to the electron shower size. It is corrected by a periodic function of the tower coordinates; after applying this correction the angular resolution obtained is $\sigma_{\theta,\phi} = (2.5/\sqrt{E/\mathrm{GeV}} + 0.25)\,\mathrm{mrad}$.

5.2 Hadron calorimeter

The hadron calorimeter serves two purposes. It is used, together with the electromagnetic calorimeter, to measure hadronic energy deposits, and it is part of the muon identification system. It consists of 23 layers of plastic streamer tubes separated by 5 cm thick iron slabs, giving a total of 7.2 interaction lengths at 90 degrees. The calorimeter is constructed from 36 modules, 24 in the barrel and 6 in each end-cap, and is read out capacitatively in 4788 projective towers with a typical tower coverage of 3.7° × 3.7°, corresponding to 4 × 4 of the electromagnetic calorimeter towers.

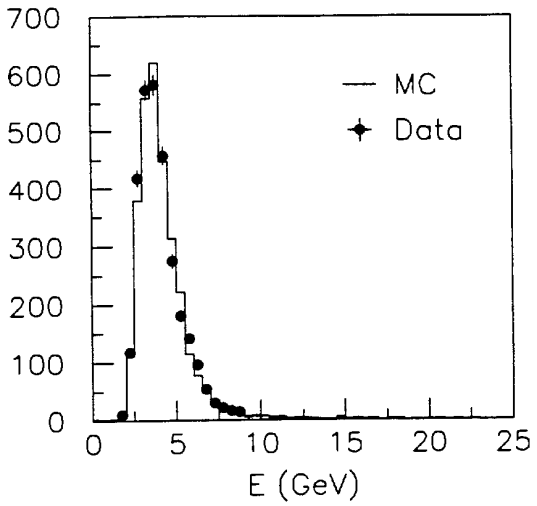

Figure 12: Distribution of the energy measured in the hadron calorimeter for muons from $Z \to \mu^+\mu^-$ events.

In addition a digital (yes or no) signal is recorded for each of the 1 cm wide tubes, providing a two-dimensional projection of the energy deposition. This is used in the identification of muons, described in Section 7 and, together with the towers, in the energy-flow algorithm, described in Section 10. Trigger signals are derived from the wires of the tubes. The time dependence of the calorimeter calibration is followed by a gas monitoring system [8] which measures variations in the calibration with a precision of about 0.4 %; variations of up to 10 % due to pressure and temperature changes have been observed over a year.

The 45 GeV muons produced in $Z \to \mu^+\mu^-$ decays are used to set the energy scale for the hadronic shower measurement, while hadronic Z decays are employed to intercalibrate the calorimeter modules. The tower responses are equalized in order to reproduce the signal of a 90 degree tower, without dead zones. The equalization has two purposes: the first is to correct for the energy loss in cracks between modules, in the barrel-endcap overlap region and at low angle; the second is to suppress the angular dependence of the signal, due to the change in sampling frequency and streamer production rate. The equalization coefficients have been calculated with a simulation tuned on test-beam data, and turn out to be roughly independent of energy in the range of interest for this experiment.

The tower information is reconstructed in the form of clusters, in a similar fashion to the electromagnetic calorimeter described in the previous section, yielding an average of 9 clusters per hadronic event. Figure 12 shows the energy distribution for muons from Z decay. The correctness of the calibration for hadronic showers has been checked using hadrons from single-prong tau decays, as shown in Figure 13 for two momentum intervals. The energy resolution of the hadron calorimeter for pions at normal incidence is

$$\frac{\sigma(E)}{E} = \frac{0.85}{\sqrt{E/\mathrm{GeV}}} \,. \tag{6}$$

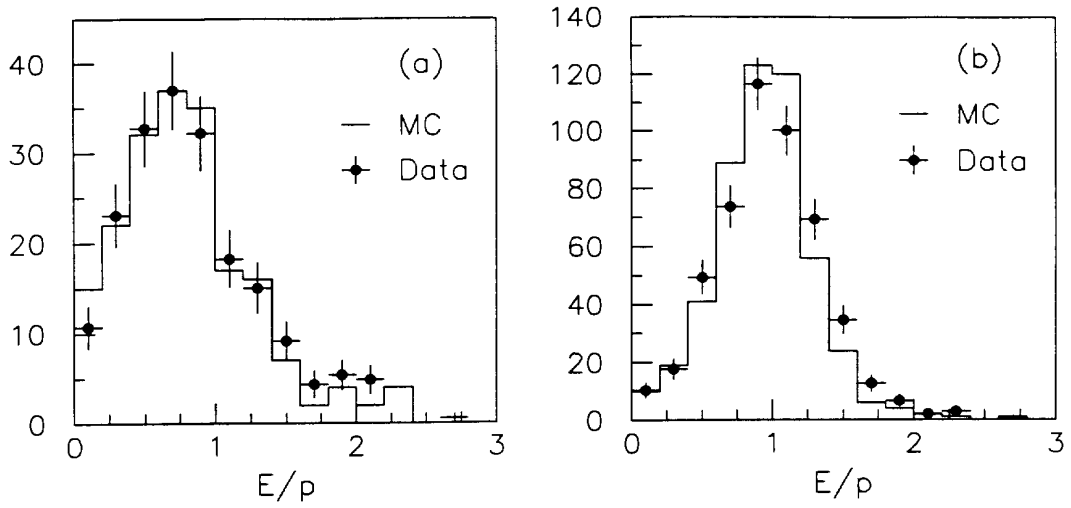

Figure 13: The ratio between the energy measured in the hadron calorimeter and the momentum measured for hadrons produced in single prong τ decays. Tracks are required to behave as minimum ionizing particles in the electromagnetic calorimeter. (a) Low momentum ($2\,\mathrm{GeV}/c < p < 5\,\mathrm{GeV}/c$), (b) high momentum ($5\,\mathrm{GeV}/c < p < 30\,\mathrm{GeV}/c$).

6 Electron identification

Electron identification is performed using two independent and complementary measurements, the dE/dx measurement from the TPC (described in Section 4) and the energy deposition measured in the electromagnetic calorimeter, compared to the track momentum and the expected shape of the shower. The basic information is expressed in terms of normally distributed estimators, on which cuts are applied to select electron candidates. The dE/dx is more effective at low momentum, and the shape of showers in the electromagnetic calorimeter at high momentum. The redundancy allows the performance of each estimator to be measured using data, over a large part of the acceptance.

6.1 Electron identification estimators

The dE/dx is measured for each track in the TPC, as described in Section 4. An estimator measuring specific ionization, R_I, is calculated by comparing the measured dE/dx, I, to that expected for an electron $\langle I \rangle$,

$$R_I = \frac{I - \langle I \rangle}{\sigma_I} \,, \tag{7}$$

where the dE/dx resolution σ_I was defined in Section 4. This is normally distributed for electrons. To ensure a reliable measurement of R_I, tracks are required to have at least 50 isolated wire hits.

The electromagnetic calorimeter has been described in the previous section. Its granularity is designed to provide good e-π separation in jets. Both the compactness of electro-

magnetic energy deposition transverse to the particle direction and the longitudinal shape of the shower are exploited, using two normally distributed estimators R_T and R_L.

Charged tracks are extrapolated from the TPC and their crossing point is computed in each of the three segments in depth of the calorimeter. The estimator R_T is defined using the four storeys closest to the extrapolated track in each segment:

$$R_T = \frac{E_4/p - \langle E_4/p \rangle}{\sigma_{E_4/p}} , \tag{8}$$

where E_4 is the total energy deposited in the selected storeys, p is the momentum of the charged track measured in the TPC, $\langle E_4/p \rangle$ is the mean energy fraction deposited by an electron in the four central towers, and $\sigma_{E_4/p}$ is the resolution expected for this ratio. The value of $\langle E_4/p \rangle$ is constant with momentum, and is measured to be 0.85 in the barrel and 0.89 in the end-caps. $\sigma_{E_4/p}$ is dominated by the resolution of the calorimeter below 25 GeV, and by that of the TPC above. The R_T estimator reflects the compactness of an electromagnetic shower and is most efficient for hadron rejection when the momentum of the track is high.

The second estimator R_L is based on the inverse of the mean position of the longitudinal energy deposition in the shower:

$$X_L = \frac{E_4}{\sum_{i=1}^{4} \sum_{j=1}^{3} E_i^j S_j} , \tag{9}$$

where E_j^i is the energy deposited in selected storey i of segment j in depth of the calorimeter, and S_j is the mean depth of energy deposition in that segment. X_L is independent of the angle of the incoming particle and is computed using the energy measured in the three segments in depth with an iterative procedure assuming, at each step, that the longitudinal deposition induced by an electromagnetic shower is described by a standard shape [9]. The normally distributed estimator R_L is defined by

$$R_L = \frac{X_L - \langle X_L \rangle}{\sigma_{X_L}} . \tag{10}$$

The momentum dependence of $\langle X_L \rangle$ and σ_{X_L} is parametrized using electrons selected in hadronic events with severe R_T and R_I cuts, and electrons originating from Bhabha events. R_L measures the degree to which the observed longitudinal shower profile matches that expected for an electron.

Figure 14 shows the distribution of R_T versus R_L for a sample of tracks enriched in photon conversions. The electron and hadron contributions are clearly separated.

6.2 Electron identification in hadronic jets

The electron identification performance is described here in the jet environment typical of hadronic Z decays. Much higher efficiency and discriminating power can be obtained for lower multiplicity leptonic decays, discussed below in Section 7.3.

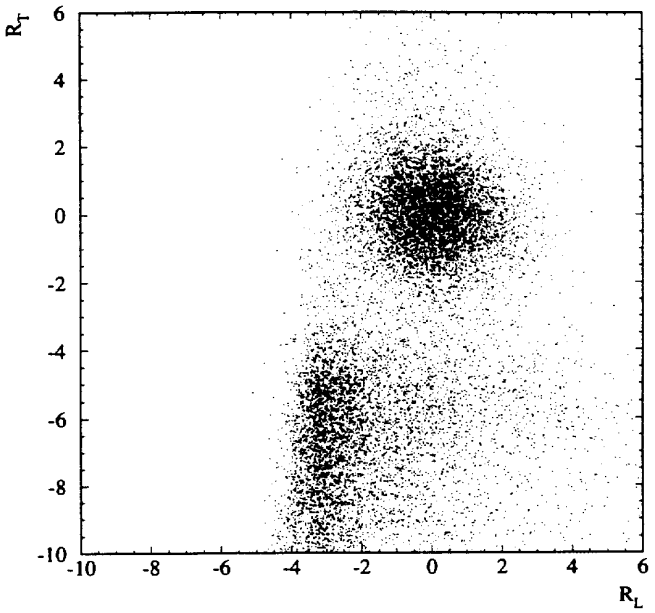

Figure 14: Electron estimators from the electromagnetic calorimeter for a sample of tracks enriched in photon conversion electrons.

Electron candidates are required to have momentum greater than $2\,\mathrm{GeV}/c$, and the following cuts are applied to the estimators: $R_I > -2.5$, $-1.8 < R_L < 3.0$, and $-1.6 < R_T$. They achieve good hadron rejection with a limited efficiency loss. No upper cut is applied on the R_T estimator because the four central towers associated to an electron can contain additional energy from a bremsstrahlung photon.

A detailed understanding of the electron identification performance is very important for some analyses, in particular for b physics, and more details about the methods used can be found in Reference [10].

For the electron identification with dE/dx the main source of inefficiency is the requirement of at least 50 isolated wire hits, for which there is a strong dependence on p, $p_\perp$ (the transverse momentum of the electron relative to its associated jet) and θ. The efficiency is measured precisely from data by counting the fraction of all electron candidates which give more than 50 wire hits, and is found to be 0.834 ± 0.002.

The electron identification efficiency using the calorimeter alone is directly measured from data using the e^+e^- pairs produced by photon materialization in the beam pipe, vertex detector, drift chamber and inner wall of the TPC. From this sample an electron purity of 98% is obtained by applying additional calorimeter and/or dE/dx electron identification cuts to the other track in the pair. The efficiency of the identification by the calorimeter is measured with respect to p, $p_\perp$ and θ of the track. No evidence for a momentum or a transverse momentum dependence of the electron identification efficiency is observed, as expected from the definition of the estimators. There is a decrease in the efficiency in the overlap and end-cap regions, due to the relatively larger size of cracks in the end-caps. The mean efficiency is 0.785 ± 0.006.

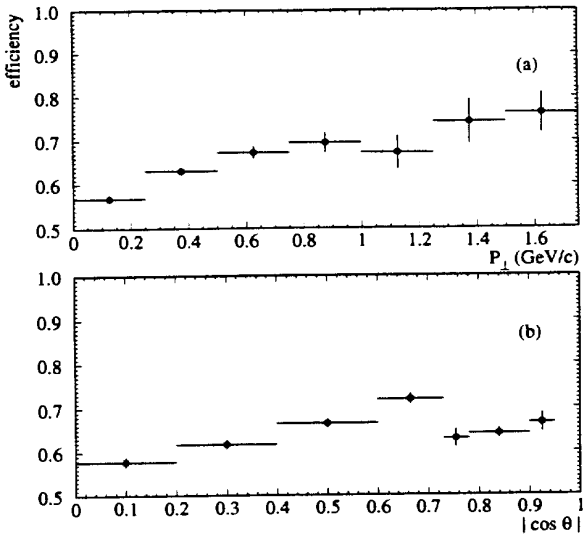

Figure 15: Global efficiency of electron identification, (a) as a function of $p_\perp$ and (b) as a function of the polar angle, when both calorimeter and dE/dx information is used.

Since the electron identification using dE/dx is independent of that using the calorimeter, the global electron identification efficiency is simply the product of the two, 0.655 ± 0.005. The $p_\perp$ and θ dependence of this efficiency is illustrated in Figure 15.

The purity of the electron sample is determined from a comparison of the information from dE/dx and from the calorimeter. The R_I distribution for electron candidates that have been selected using the calorimeter is shown in Figure 16. It is the sum of two parts, which are measured from the data as a function of p and $p_\perp$: a fitted Gaussian which gives the shape of the electrons in this sample, and a contribution from hadrons, the shape of which is taken from tracks which are selected as hadrons in the calorimeter. From these two distributions the hadronic contamination is estimated, and the probability of misidentifying a hadron as an electron is calculated. The mean value is $(3.44 \pm 0.05) \times 10^{-3}$, and if the dE/dx cut ($R_I > -2.5$) is included this value becomes $(0.95 \pm 0.03) \times 10^{-3}$.

7 Muon identification

Muons are identified by making use of the tracking capabilities of the hadron calorimeter, together with the muon chamber information. Muon identification in the calorimeter uses the digital readout (described in Section 5.2) to check whether particles penetrate through the whole depth of the calorimeter.

Tracks are extrapolated (as if they were a muon) through the calorimeter material taking into account a detailed magnetic field map and estimated energy losses. A 'road' is opened around the extrapolated track, with a width of three times the estimated extrapolation uncertainty due to multiple scattering. A calorimeter plane is said to be expected to fire if

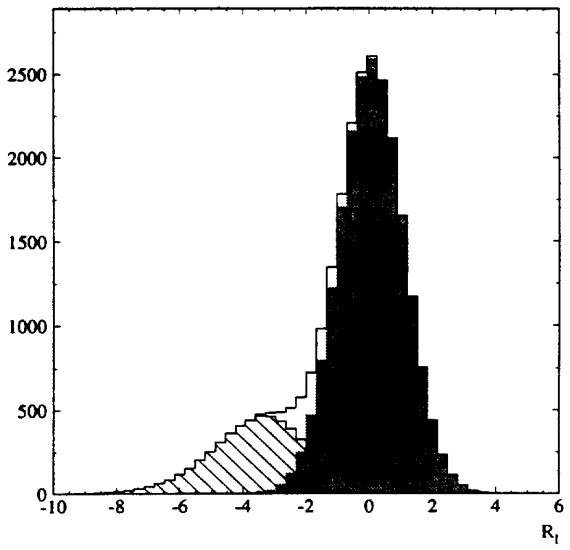

Figure 16: R_I distribution for electron candidates which have been selected using calorimetric information. The hatched part represents the hadronic contamination, and the shaded part electrons.

the extrapolated track intersects it within an active region, and the plane is said to have fired if a digital hit lies within the multiple scattering road. For a hit to be counted, the number of adjacent firing tubes must not be greater than three.

The hadron calorimeter is surrounded by two double-layers of muon chambers separated by 50 cm, located behind the last iron slab of the calorimeter, which is at 8 hadronic interaction lengths from the interaction point. Each double-layer has two planes of streamer tubes and each plane reads out two orthogonal coordinates using aluminium strips. The two sets of coordinates of a double-layer are combined to yield a space point. A track is defined to have hit the muon chambers if at least one of the two double-layers yields a space point whose distance from the extrapolated track is less than four times the estimated standard deviation from multiple scattering.

7.1 Muon identification in hadronic jets

Tracks are considered for muon identification in hadronic jets if their momentum is greater than 3 GeV/c. The identification is performed by selecting tracks that penetrate through the whole depth of the hadron calorimeter without showering. The identification efficiency does not vary significantly with momentum, since a muon with momentum above 3 GeV/c escapes the detector, and test-beam data show that the efficiency of the tubes is independent of momentum.

The cuts used to define a penetrating track are: $N_{fire}/N_{exp} \geq 0.4$, $N_{exp} \geq 10$, and $N_{10} > 4$, where N_{fire}, N_{exp} and N_{10} are, respectively, the number of actually firing planes, the number of expected planes, and the number of firing planes within the last ten expected

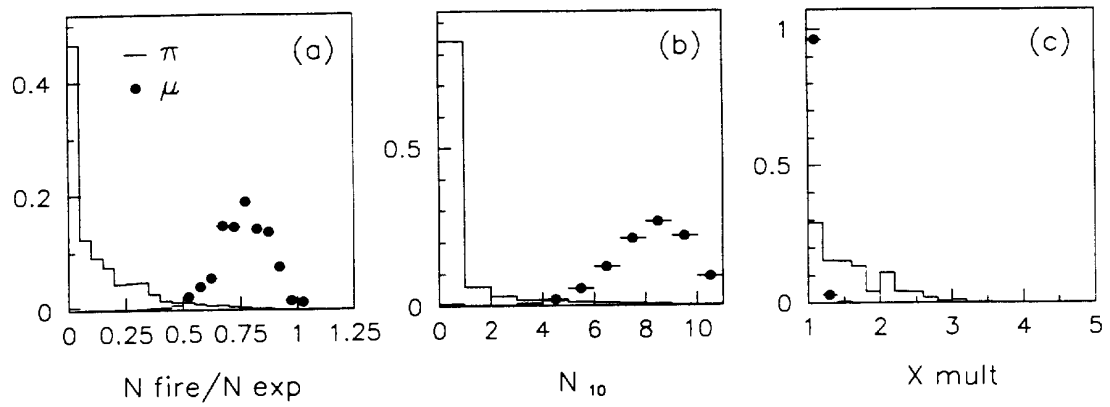

Figure 17: Distribution of (a) N_{fire}/N_{exp}, (b) N_{10} and (c) X_{mult}, for muons (points) and pions (solid line), with N_{exp} greater than 10. The plots have been normalized to equal areas, and the vertical scale is arbitrary.

for the track. These cuts select penetrating particles and are suitable for isolated muons. To enhance the rejection power against hadron background the typical features of the digital pattern created by a hadron shower in the hadron calorimeter are used in addition. The number of digital hits in the last eleven planes of the calorimeter within a wide 'road' (increasing from 20 cm to 30 cm width) around the extrapolated track is divided by the number of firing planes to give a variable X_{mult} that represents the average hit multiplicity per fired plane. The cut applied for muon identification is $X_{mult} < 1.5$; this removes about 1 % of the prompt muons. In Figure 17 the distributions of N_{fire}/N_{exp}, N_{10} and X_{mult} for muons coming from $Z \to \mu^+\mu^-$ events are compared to those of pions produced in τ decay.

The requirement of the associated hits in the muon chambers, in addition to the hadron calorimeter criteria, is powerful for background rejection. The Monte Carlo simulation predicts that while about 94 % of the muons which have been identified in the calorimeter are associated to a muon chamber hit, only about 20 % of the misidentified hadrons are associated. This is due to the two-dimensional nature of the muon chamber hits, compared to the one-dimensional strips in the calorimeter, and also to the demand that the particle has passed through all the iron.

Due to the high track multiplicity inside a jet and the fact that the calorimeter tracking is only in one projection, the multiple scattering 'roads' opened around different tracks can overlap, and the same hit can be associated to more than one track. When two tracks have common hits and both are identified as muons, a choice has to be made. Usually the muon chambers with their two-dimensional points resolve the ambiguity; when both tracks share exactly the same muon chamber hits, the one with the minimum hit-to-track distance is chosen. The fraction of prompt muons lost due to this algorithm is about 0.4 %.

7.2 Muon identification performance

The hadron calorimeter plane efficiency is mapped in detail in the ALEPH Monte Carlo simulation, using $Z \to \mu^+\mu^-$ events that have been selected by requiring the presence of

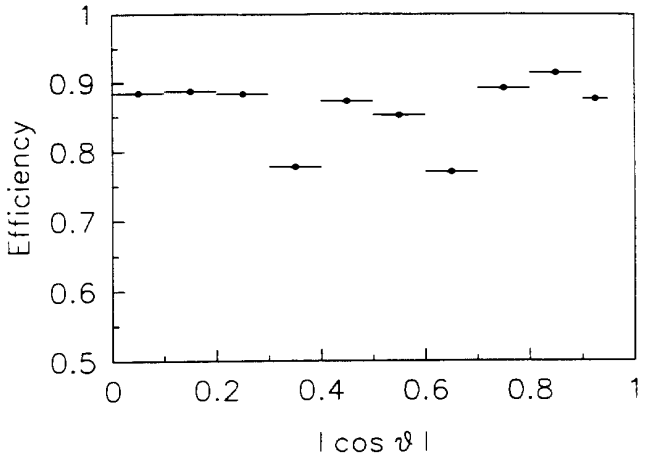

Figure 18: Efficiency of the muon selection as a function of $\cos\theta$ for isolated muons. The two lower efficiency points correspond to the magnet support legs which are not instrumented with muon chambers.

less than six charged tracks and using an algorithm that makes use of the tracking and electromagnetic calorimeter information to reject the other leptonic Z decays. The statistical precision obtained on the plane efficiency is about 1 % for the barrel and 2 % for the end-caps, and the average plane efficiency is about 75 %. The inefficiency is due to the presence of plastic walls between tubes (13 %), geometrical dead zones within the planes (7 %), and readout inefficiencies (5 %).

The efficiency of the muon chambers has been measured with a procedure similar to that used for the calorimeter, and has an average value of 92 %. Requiring that at least one muon chamber hit is associated to the candidate selected using the hadron calorimeter information, the dependence on polar angle of the resulting muon identification efficiency is shown in Figure 18, measured using isolated muons. The two dips in the efficiency are due to the magnet supporting legs which are not instrumented with muon chambers. The average muon identification efficiency is 86 %.

The probability of misidentifying a hadron as a muon in hadronic Z decays is about 0.8 %, half of which is due to hadron punch-through and the rest to pion and kaon decays within the TPC volume.

7.3 Charged particle identification in τ decays

When charged particles are well isolated from other particles, more optimized identification methods can be used. In τ decays, the dominant one-prong topology (86 %) allows the construction of a full likelihood using distributions of discriminating variables for each particle type from dE/dx, electromagnetic calorimeter (R_T, R_L), hadron calorimeter (average shower width and penetration, both using the tube readout) and the muon chambers (hit multiplicity). The principle of the method and some early results are given in Reference [11]. The present performance, given in Table 2 for particles in the 2–45 GeV/c momentum range, shows that high efficiencies and low misidentification rates can be simultaneously achieved.

Table 2: Identification matrix from a likelihood method used in the analysis of τ decays. The quoted efficiencies (in %), obtained from a Monte Carlo simulation, agree well with experimental results from samples of tagged particles from well-identified processes (Bhabhas, μ-pairs, $\gamma\gamma$-induced lepton-pairs and pions from hadronic τ decays using π^0 tagging).

	True particle type		
Identified	e	μ	hadron
e	99.60	< 0.01	0.61
μ	< 0.01	99.46	0.87
hadron	0.40	0.54	98.52

8 Photon and π^0 identification

The three-dimensional segmentation of the electromagnetic calorimeter allows a good spatial resolution to be achieved for photons and π^0's up to the highest energies available at LEP. However, the clustering algorithm described in Section 5.1 builds big clusters, often merging energy from photons and hadronic interactions. Consequently a method has been devised to identify and reconstruct photons and π^0's which is better adapted to hadronic Z decays and is applied to the clusters defined in Section 5.1. It uses the facts that electromagnetic showers generally start in the first segment in depth of the electromagnetic calorimeter and that, unlike the cell patterns of hadronic clusters, storeys receiving energy from a photon have a compact arrangement and most of them share a face with another storey associated to the same photon.

8.1 Photon identification

The storeys of the first segment in depth of the electromagnetic calorimeter are scanned in the order of decreasing energy. A storey without a more energetic neighbour defines a new cluster. Other storeys are assigned to the cluster of their highest energy neighbour. To take advantage of the compact nature of electromagnetic showers and of the projective geometry of the calorimeter two storeys are considered neighbours only when they share a common face. The same procedure is then applied to the storeys of the second and third segments in depth but then, when processing a storey, the algorithm looks first for a neighbour in the previous segment. The clusters found by the algorithm are retained as candidate photons if their energy is greater than 0.25 GeV and if there is no charged track impact at a distance of less than 2 cm from the cluster barycenter.

The position of a photon impact point is computed in two steps. A first approximation is given by the cluster barycentre i.e. the energy-weighted mean of the coordinates of each storey centre. This position is corrected for the finite size of the calorimeter cells using the parametrization of the S-shape curve described in Section 5.1.

In order to reduce the sensitivity of the energy measurement to hadronic background and clustering effects, the photon energy is computed from the energy collected in the four central

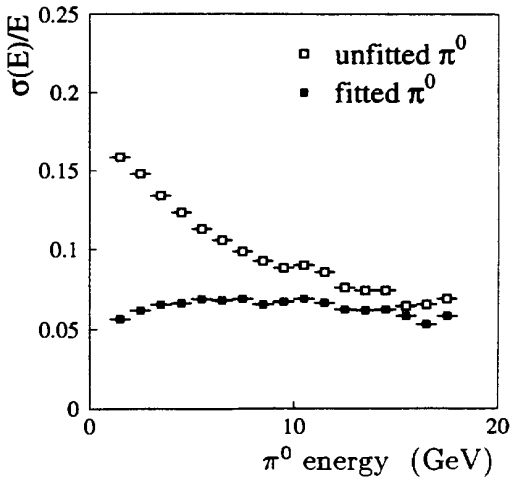

Figure 19: Resolution on the π^0 energy before and after kinematic fit.

towers of the cluster, and the expected value of the fraction of energy in the four towers, F_4. This fraction is computed from the parametrization of the shower shape for a single photon in the calorimeter. The computation takes into account the calorimeter pad area and the distance between the photon impact and the nearest tower corner, as well as the variation with energy of the expected F_4. Corrections to the energy are computed for energy losses before and after the calorimeter and energy loss in the overlap using the methods presented in Section 5.1.

The angular resolution for an isolated cluster is the same as that described in Section 5.1. The use of only a part of the storeys to measure the energy degrades the energy resolution to $\sigma(E)/E = 0.25/\sqrt{E/\mathrm{GeV}}$ instead of the $0.18/\sqrt{E/\mathrm{GeV}}$ of Section 5.1. The efficiency and background depend strongly on the density of particle impacts on the calorimeter.

8.2 π^0 reconstruction

The 4-momenta of π^0 candidates are obtained by adding the photon momenta when the $\gamma\gamma$ invariant mass is compatible with a π^0 mass. The energy resolution of the π^0 is then limited by the energy resolution of the calorimeter. It can be greatly improved by using the kinematical constraint of the π^0 mass. Two cases are distinguished. At energies below 10 GeV the two γ clusters are well separated in the calorimeter and the error on the π^0 opening angle is small compared to the error on the γ energies. A fit is then performed keeping the opening angle constant and constraining the $\gamma\gamma$ mass to m_{π^0}. For high energy π^0's the two γ clusters are adjacent. The clustering algorithm described above induces a bias in the sharing of storeys between the two clusters which increases the asymmetry of the π^0. In order not to bias the fitted energy, variation of the opening angle is allowed in the fitting procedure. Figure 19 shows that the π^0 fit greatly improves the energy reconstruction. The final resolution $\sigma(E)/E$ is about 6.5 %, almost independent of the energy. In τ decays with two identified photons the invariant mass of the photons is shown in Figure 20, displaying a clean π^0 signal.

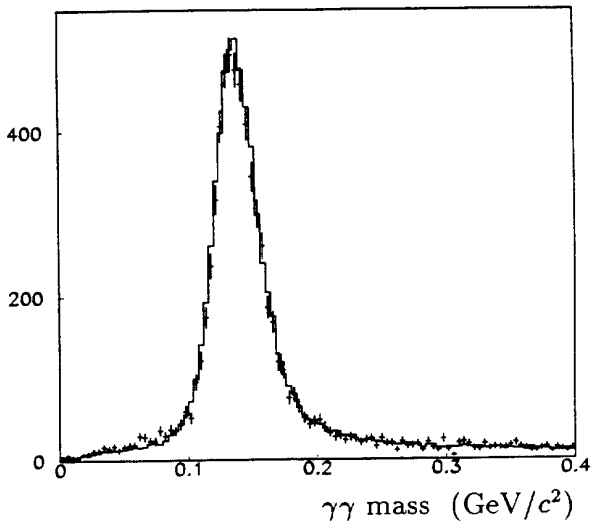

Figure 20: Two-photon invariant mass spectrum in τ decays where the total photon energy is greater than 3 GeV; the data are shown as points with error bars and the Monte Carlo simulation is shown as a histogram. The mean π^0 energy in this figure is 10 GeV.

Figure 21 shows the π^0 selection efficiency in hadronic events as a function of the energy. The probability to resolve a π^0 into two γ clusters decreases for energies greater than 10 GeV. Further information is contained in the distribution, within a single cluster, of the energy in the calorimeter. To extract it, energy weighted moments $\sum_i E_i x_i^n / \sum_i E_i$ of the two dimensional energy distribution are computed. Assuming that the cluster contains only two photons, by using moments up to the third order it is possible to reconstruct the two γ momenta and compute their effective mass. The effective mass spectrum of Figure 22 displays a broad π^0 peak and shows that the method allows a check of the π^0 hypothesis for unresolved high energy clusters.

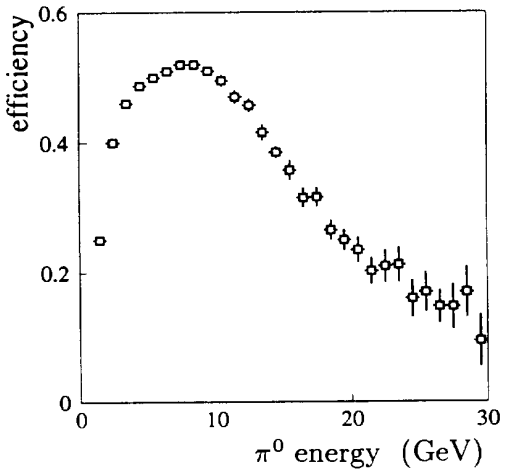

Figure 21: Selection efficiency for π^0's in hadronic events, with resolved photons.

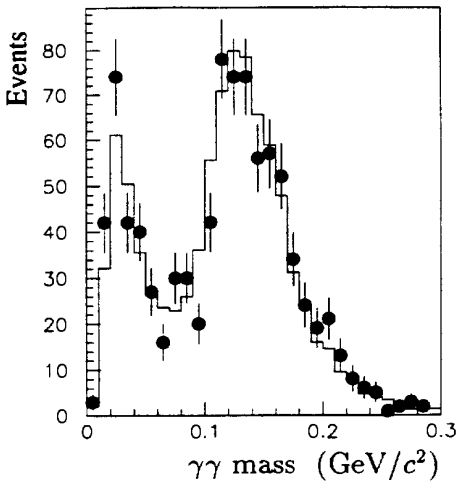

Figure 22: Effective mass reconstructed from moment analysis in a sample of τ decays with one charged hadron and one cluster of energy greater than 4 GeV. The points are for data and the histogram is for Monte Carlo simulation; the mean π^0 energy in this figure is 20 GeV.

9 V^0 identification

Photons traversing the detector material placed prior to the electromagnetic calorimeter may convert into an electron-positron pair, and will therefore not be identified as described in the previous section. Since the resulting charged particle tracks do not originate from the main interaction point, they will be rejected as 'bad tracks' in many analyses. This also applies to neutral particles (K^0_s and Λ) that decay into a pair of charged particles inside the tracking volume. Such decays are denoted V^0's.

In order to identify V^0's an algorithm has been developed that searches for secondary vertices as follows: V^0 candidates are selected considering all pairs of oppositely charged particle tracks having at least five TPC hits, with at least one of the pair not coming from the primary vertex. An approximate vertex position is found from the intersection of the two helices projected onto the plane perpendicular to the magnetic field. A three-dimensional vertex fit is then performed without kinematical constraints using the approximate vertex position as starting point of the fit; further details can be found in Reference [12].

Although the algorithm is aimed at reconstructing any secondary vertex, its performance can be simply studied with particles of known mass: K^0_s and Λ. In order to reduce the combinatorial background, cuts are applied on the three-dimensional distance of each track from the approximate vertex position, on the χ^2 of the vertex fit and on the angle between the V^0 flight direction and its momentum. The invariant mass of the V^0 is computed for the three decay hypotheses: $K^0 \to \pi^+\pi^-$, $\Lambda \to p\pi^-$ and $\overline{\Lambda} \to \pi^+\overline{p}$. The reconstructed mass distributions are shown in Figure 23 for V^0's reconstructed with low momentum charged particles. Candidates are accepted if the mass agrees with one of the three hypothesis within three standard deviations. Before the use of dE/dx about 5 % of K^0's are ambiguous with Λ ($\bar{\Lambda}$) and 15 % of Λ's are ambiguous with K^0.

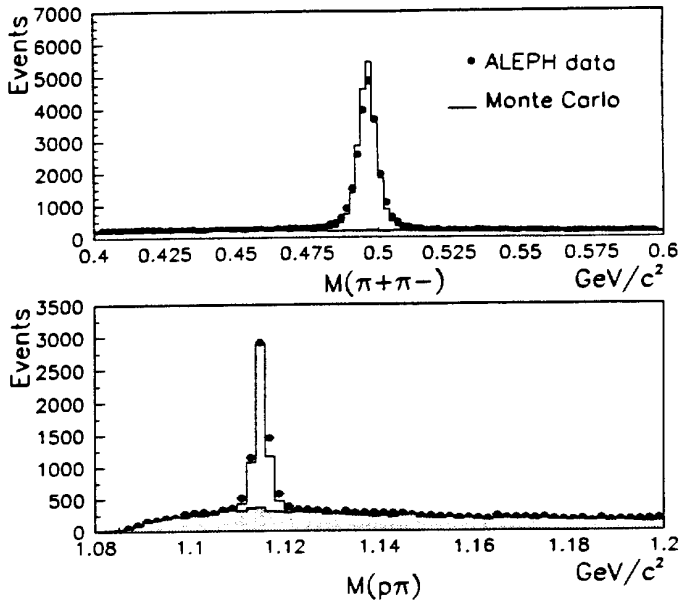

Figure 23: V^0 mass distributions around (a) the K^0 and (b) the Λ masses, for low momentum V^0's (1.4 GeV/c < p < 2.7 GeV/c).

The efficiency of this selection has a strong dependence on the V^0 momentum: it is maximal for momenta of about 8 GeV/c. At low momenta the main causes of loss are the cut on the minimum transverse momentum of the decay products with respect to the beam axis, implicitly applied by requiring at least five TPC hits, and the incompatibility of at least one track with the primary vertex. At high momenta the loss of efficiency is due to the finite tracking volume and to the two-track separation capability of the TPC. The efficiency is evaluated using a sample of simulated hadronic decays of the Z. Depending on the optimization of the cuts typically 50 % (42 %) of generated $K^0 \to \pi^+\pi^-$ ($\Lambda \to p\pi^-$) are reconstructed with a purity of 80 % (50 %).

10 Energy flow determination

The simplest way to determine the energy flow of an event recorded in the ALEPH detector is to make the sum of the raw energy found in all calorimetric cells without performing any particle identification. This method yields a resolution of $\sigma(E)/E = 1.2/\sqrt{E/\mathrm{GeV}}$ for hadronic decays of the Z. In order to improve the resolution, an energy flow reconstruction algorithm has been developed making use of track momenta and taking advantage of the photon, electron and muon identification capabilities. Before being superseded by the tungsten/silicon calorimeters described in the next section, the luminosity was measured in ALEPH using forward calorimeters of similar construction to the electromagnetic calorimeter. These are still installed, and for the purpose of energy flow they are treated as a part of the electromagnetic calorimeter, extending the solid angle coverage down to 40 mrad.

10.1 Description of the method

In a first stage, hereafter called cleaning, the following selection of charged particle tracks and calorimeter clusters is made in order to reject, as far as possible, those originating from the rare misbehaviours of the front-end electronics, the data acquisition system or the reconstruction chain.

1. The charged particle tracks, reconstructed using the information of the vertex detector, the drift chamber and the TPC as described in Section 3, are required to have at least four hits in the TPC and to originate from within a cylinder of length 20 cm and radius 2 cm coaxial with the beam and centred at the nominal collision point. If the reconstructed momentum is in excess of 15 GeV/c at least eight points are required in the TPC, and one in the drift chamber.

2. The charged particle tracks rejected by this selection are recovered if they belong to a reconstructed V^0 (see Section 9) compatible with originating from the nominal collision point within a cylinder of length 30 cm and radius 5 cm coaxial with the beam. The tracks that also fail this requirement are ignored in the following.

3. The noisy channels of the electromagnetic and hadron calorimeters, appearing systematically in many consecutive events, are located prior to the event reconstruction and are not used in the cluster finding. The fake energy deposits due to occasional noise in the towers of the calorimeters are detected and removed when the corresponding signal is incompatible with the signal measured independently on the wire planes.

The efficiency of the last step of this cleaning procedure can be tested on events randomly triggered where no signal should be present. Among 30,000 such events it can be seen that a third of them actually contain a fake signal in the calorimeters, with a mean value of 1 GeV and a maximum larger than 30 GeV, as shown in Figure 24. In the same figure the energy distribution is shown after the cleaning stage: no energy remains in 98 % of these events, the mean energy becomes 15 MeV per event and the maximum does not exceed 3.5 GeV. In Section 10.2 it is shown that the real signal is not noticeably harmed by this efficient cleaning stage, made possible by the redundancy in the readout of both calorimeters.

After the cleaning the charged particle tracks are extrapolated to the calorimeters, and groups of topologically connected tracks and clusters (called 'calorimeter objects') are formed. Each calorimeter object is then processed using the following steps.

1. All the charged particle tracks coming from the nominal interaction point or belonging to a reconstructed V^0, within the tolerances presented above, are counted as charged energy assuming they are pions.

2. The charged particle tracks identified as electrons, as described in Section 6, are removed from the calorimeter object, together with the energy contained in the associated electromagnetic calorimeter towers. If the difference between this calorimeter energy and the track momentum is larger than three times the expected resolution, this difference is assumed to come from a bremsstrahlung photon, and is counted as neutral electromagnetic energy.

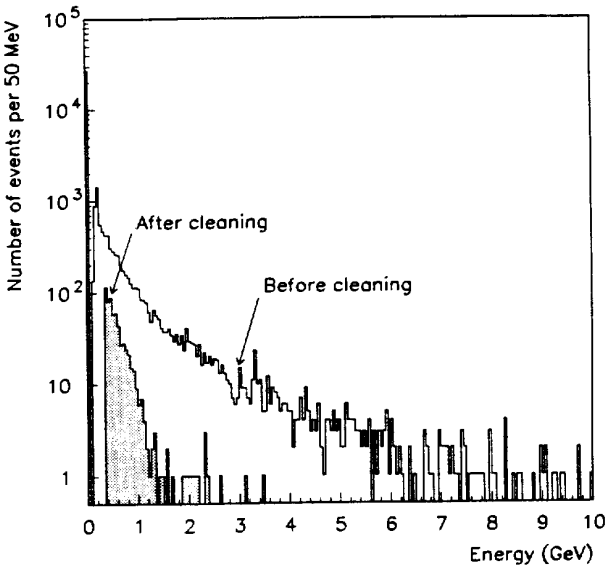

Figure 24: Energy distributions for events randomly triggered, before (empty histogram) and after (shaded histogram) cleaning. The gap after cleaning at low energy results from the energy threshold for identifying photon clusters.

3. The charged particle tracks identified as muons, as described in Section 7, are removed from the calorimeter object, together with a maximum of 1 GeV from the closest associated electromagnetic calorimeter cluster (if any) and a maximum of 400 MeV per plane fired around the extrapolation of the muon track from the corresponding hadron calorimeter cluster.

4. The photons and π^0's, identified as presented in Section 8, are counted as neutral electromagnetic energy and are removed from the calorimeter object.

5. At this stage, the only particles left in the calorimeter object should be charged and neutral hadrons. The charged hadron energy has already been determined in the first step, but the neutral hadron energy has not been accounted for. Although possible in principle via a specific tube pattern recognition, a direct identification of neutral hadrons is difficult and has not yet been attempted for the energy-flow reconstruction. Here, a neutral hadron is identified as a significant excess of calorimetric energy: in a given calorimeter object, already processed as explained above, the remaining energy left in the calorimeters is summed, after first scaling that from the electromagnetic calorimeter by the ratio of the calorimeter's response to electrons and pions. If this sum exceeds the energy of any remaining charged particle tracks, and the excess is both larger than the expected resolution on that energy when measured in the calorimeters, and greater than 500 MeV, then it is counted as neutral hadronic energy. The ratio of the electromagnetic calorimeter's response to electrons and pions has been determined to be ~ 1.3 with test-beam data. However, in order to account for the fact that low energy photons often escape identification in the preceding step of this analysis, the ratio is modulated according to the penetration of the particle and is taken as 1.0, 1.3 and 1.6 in the first, second and third segments in depth of the calorimeter, respectively.

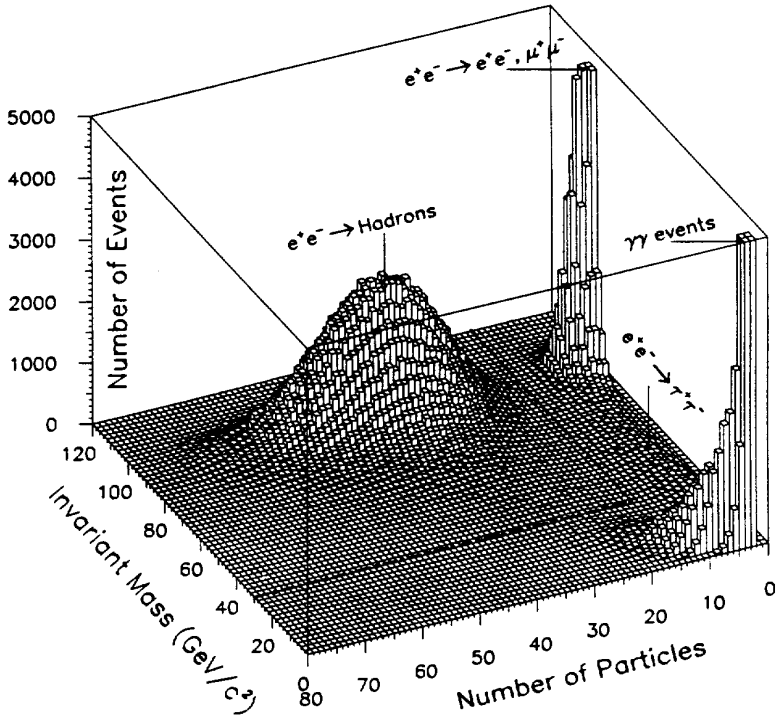

Figure 25: Invariant mass versus number of particles for all the events with at least two charged particle tracks, from part of the 1992 ALEPH data. The two low-multiplicity peaks have been truncated.

This is repeated for all the calorimeter objects of the event and results in a set of 'energy-flow objects' (electrons, muons, photons, charged or neutral hadrons), also called particles in the following, characterized by their energies and momenta. To this list are added all the clusters found in the luminosity monitor, where no particle identification is available. This list is expected to be a close representation of the reality, i.e. of the stable particles actually produced by the collision. Since the neutrinos escape undetected, they cannot be in the list but they should be detected indirectly by the presence of missing energy in the event.

10.2 Performance of the reconstruction

A qualitative impression of the performance of the energy-flow reconstruction can be seen in Figure 25, obtained with data taken at the Z peak. In this figure the distribution of the total invariant mass is shown as a function of the number of energy-flow objects for all the events containing at least two charged particles. As a first application, this provides a very simple way to efficiently separate hadronic events from dilepton events and $\gamma\gamma$ collisions: requiring at least 15 energy-flow objects and an invariant mass in excess of $30\,\mathrm{GeV}/c^2$ leads to a selection efficiency of 99.6 % with a residual contamination smaller than 0.4 % coming from $e^+e^- \to \tau^+\tau^-$ events and from $\gamma\gamma$ collisions. These two criteria are indicated by a dash-dotted line in Figure 25.

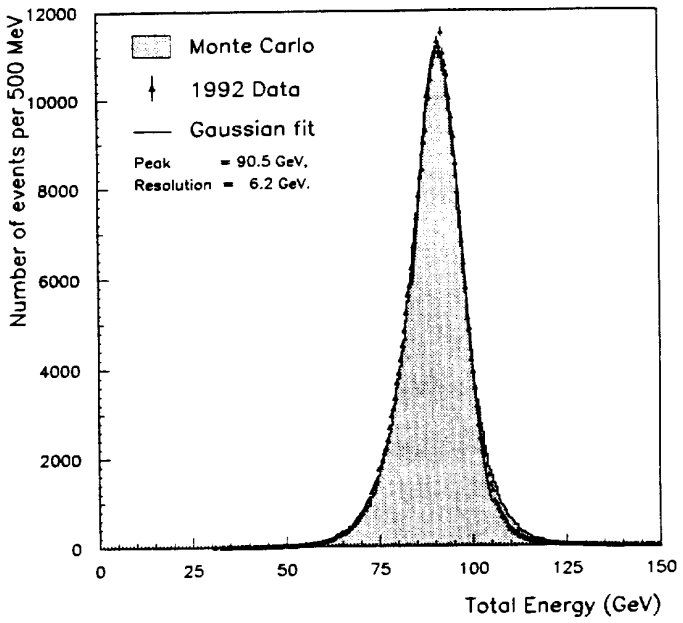

Figure 26: Distribution of the total energy for well-contained hadronic events for the 1992 data (points) and Monte Carlo (shaded histogram).

More quantitatively, the energy-flow resolution can be determined from the data using this sample, which corresponds to $\sim$700,000 hadronic events selected as explained above. Non-central events (i.e. with any energy within 12° of the beam axis, or with more than 10 % of the total energy within 30° of the beam axis) are removed, in order to avoid energy losses around the beam direction. The total energy distribution thus obtained is shown in Figure 26 and is fitted to a Gaussian above 85 GeV in order to be free of tails from energy losses not due to the detector or the algorithm itself (such as, for instance, initial state radiation or lost neutrino energy in the semileptonic decays of heavy quarks).

The Gaussian fit gives a peak value of 90.5 GeV (62 % from charged particles, 25 % from photons and 13 % from neutral hadrons), with a resolution of 6.2 GeV. It is well reproduced by a sample of 700,000 fully simulated hadronic events in which a peak value of 90.7 GeV and a resolution of 6.5 GeV are obtained (see Figure 26). This way of measuring the resolution was also verified using the simulated events by directly comparing the energy reconstructed by the energy flow algorithm to the expectation in the case of a perfect detector. A resolution on the difference of 6.5 GeV is also obtained.

A similar technique has been applied to simulated data to measure the expected jet angular resolution, by comparing the directions of the original partons to the directions of the reconstructed jets, with both a perfect and a fully simulated detector. Only two-jet events with jet masses smaller than 15 GeV/c^2 have been considered here in order to minimize wrong particle-parton associations when dividing the events into two hemispheres by a plane perpendicular to the thrust axis. The resolutions thus obtained, shown in Figure 27, are 18 mrad for the polar angle and 19 mrad for the azimuthal angle, half of which is due to the wrong associations of slow particles and to the neutrinos produced in the hadronization

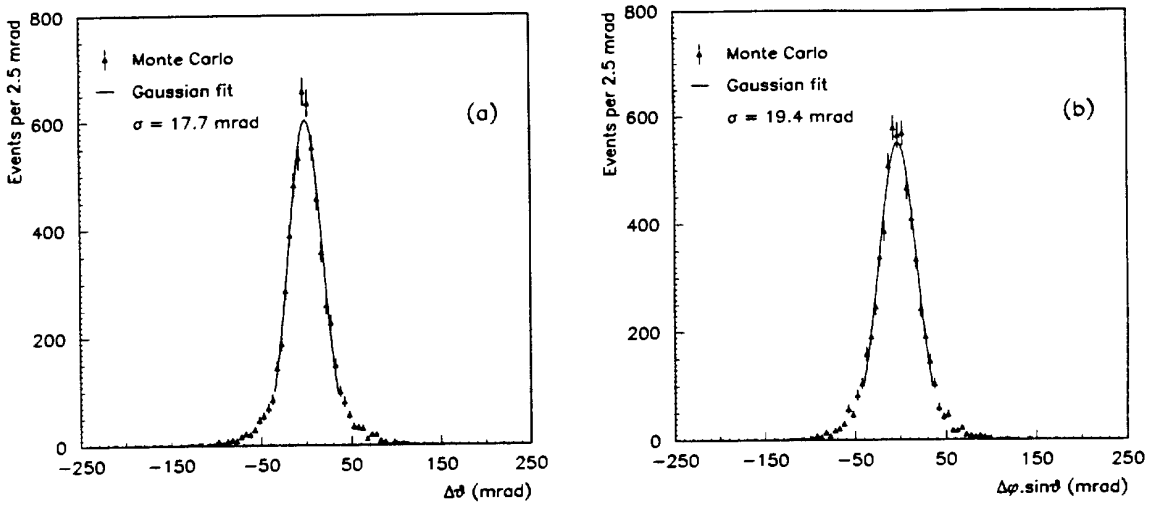

Figure 27: Jet-angular resolution as determined by Monte Carlo simulation for hadronic two-jet events, for (a) the polar and (b) the azimuthal angle.

and decay processes, also responsible for the small non-Gaussian tails of the distributions. These effects would survive with a perfect detector, and become dominant for heavier jets (i.e. when hard gluon radiation occurs).

10.3 Calibration of the algorithm

In Section 10.2 the energy resolution and the absolute calibration have only been obtained at one point, namely at $\sqrt{s} = 91.2\,\mathrm{GeV}$. In order to check the resolution and the calibration of the algorithm for other energy values, a control analysis has been performed with hadronic events accompanied by an isolated, energetic photon (or a π^0) coming either from initial/final state radiation or from the hadronization itself. Such an event is shown in Figure 28.

The selected hadronic events have to be well-contained in the detector as defined in the previous section. They must have a photon with an energy in excess of 20 GeV, and two jets are formed with the remaining hadronic system. To be isolated, the photon is required to form an angle larger than 20° with each of the two jet directions and the photon-jet invariant masses must exceed $10\,\mathrm{GeV}/c^2$. These events provide two methods for the determination of the invariant mass of the hadronic system: the direct determination of the visible mass m_{vis} using the energy flow algorithm, and the computation of the mass m_{rec} recoiling against the well-determined photon energy E_γ. Since this mass is given by $m^2_{rec} = s - 2E_\gamma\sqrt{s}$, the method allows hadronic masses below $70\,\mathrm{GeV}/c^2$ to be tested.

The distribution of $\Delta m = m_{vis} - m_{rec}$ obtained with the 3525 such events found in the ALEPH data taken since 1989 is well compatible with that obtained from fully simulated hadronic events, as shown in Figure 29 (a). The peak value of $(-0.35 \pm 0.20)\,\mathrm{GeV}/c^2$ confirms the validity of the absolute calibration, already observed at 91.2 GeV, over a wide energy domain.

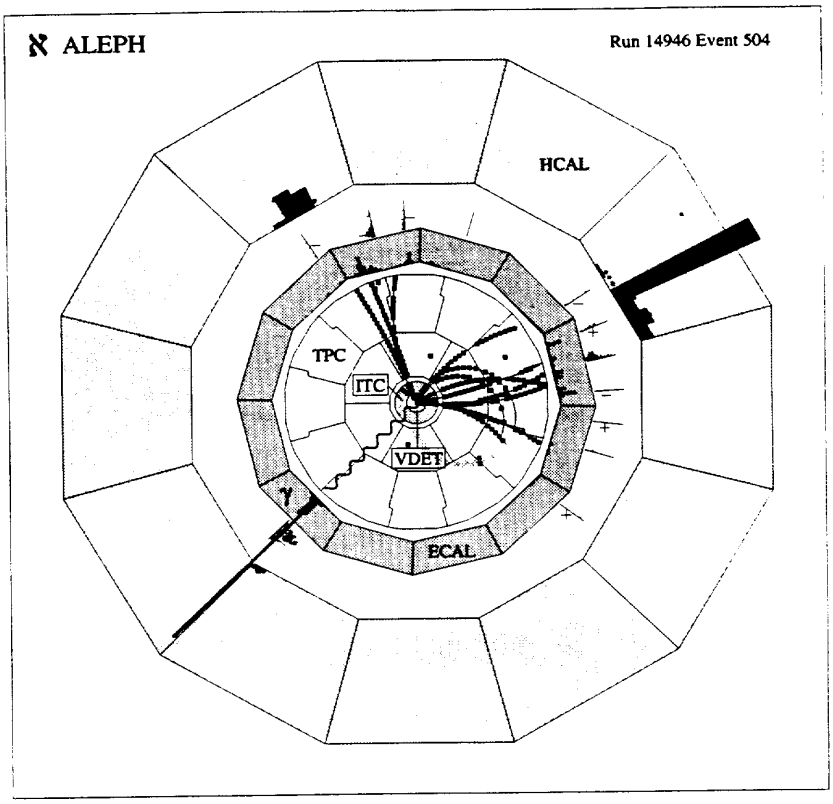

Figure 28: An hadronic event accompanied by an isolated, energetic photon, represented by a wiggly line, carrying an energy of (30.8 ± 1.1) GeV. The mass recoiling against the photon is $(52.0 \pm 1.9)\,\mathrm{GeV}/c^2$, while the visible mass of the hadronic system is $(53.6 \pm 4.9)\,\mathrm{GeV}/c^2$.

Since the resolution achieved for m_{rec} depends strongly on the hadronic mass (see Figure 29 (b)), the event sample has been divided into several subsamples, each corresponding to a given value of m_{rec} within $\pm 5\,\mathrm{GeV}/c^2$ (except for events with mass smaller than $40\,\mathrm{GeV}/c^2$, regrouped into a single subsample). From the resolution measured on Δm, it is then possible to compute the resolution on m_{vis} by unfolding the contribution from the resolution on m_{rec}. The result is shown in Figure 29 (b) where the point obtained at 91.2 GeV has also been drawn. The dependence of the resolution on the energy is governed by the calorimeter performance and is expected to vary with $\sqrt{E}$. This resolution is well reproduced by the following parametrization:

$$\sigma(E) = (0.59 \pm 0.03)\sqrt{E/\mathrm{GeV}} + (0.6 \pm 0.3)\ \mathrm{GeV}\ . \tag{11}$$

If the ALEPH particle identification capabilities were perfect, the tracking and calorimetry performances are such that a resolution of ~ 3 GeV could be achieved for the total energy measured in hadronic events at 91.2 GeV.

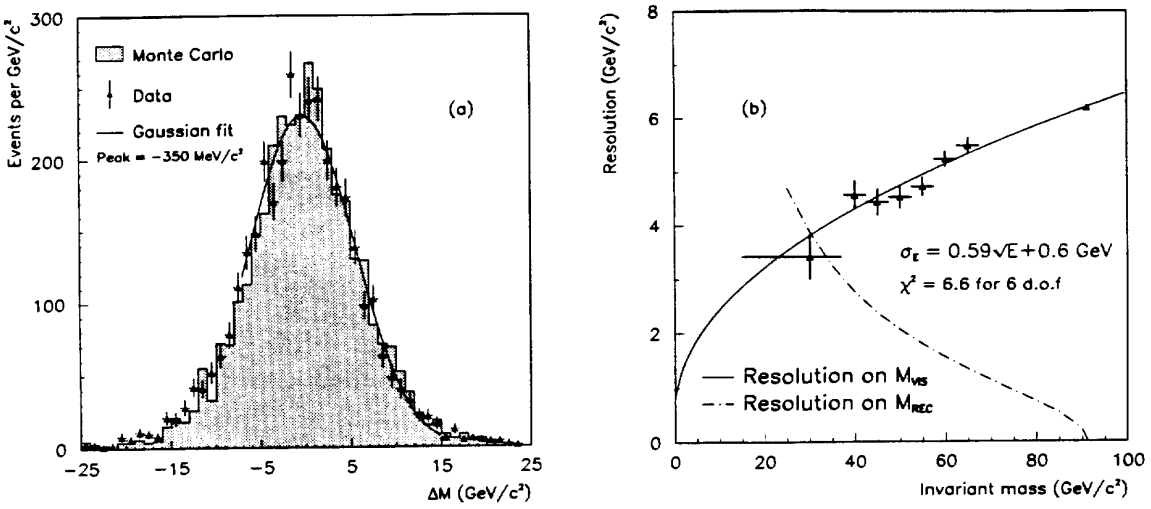

Figure 29: (a) Distribution of Δm (see text) for hadronic events accompanied by an isolated, energetic photon, both for data and Monte Carlo. (b) Evolution of the resolution on m_{vis} (points with error bars) and m_{rec} (dash-dotted line) with the hadronic mass. Also indicated (full line) is the result of the fit to a calorimetric-like resolution.

11 Luminosity measurement

The luminosity is determined from the measurement of small-angle elastic (Bhabha) scattering, for which the cross-section is well known, into a precisely defined fiducial region. In ALEPH, since 1992, the luminosity detectors are two tungsten/silicon calorimeters covering the 24–58 mrad angular interval. The units are twelve-layered sandwiches of tungsten and silicon wafers. Each silicon layer is read out on 512 pads, corresponding to 16 radial pad-rows of 5.225 mm width, and 11.25° segmentation in azimuth. Successive layers are rotated by one third of 11.25°. This construction permits the assembly of each of the detectors without azimuthal cracks. The energy resolution for electrons is $\sigma(E)/E = 0.33/\sqrt{E/\mathrm{GeV}}$. Details may be found in Reference [13].

11.1 Luminosity event selection

Bhabha events are selected as follows.

1. At least one reconstructed cluster is required on each side. Since Bhabha events generally have radiated photons which may or may not be distinguishable from the 'primary' cluster, no upper limit on the number of clusters found is imposed. Most of the events (97.5 %) have ≤ 3 reconstructed clusters.

2. The energy of the largest cluster on each side must exceed 44 % of the beam energy (> 20 GeV at the peak) in order to ensure trigger efficiency, and their sum must exceed 60 % of the c.m.s. energy (55 GeV at the peak), to separate the Bhabha signal from

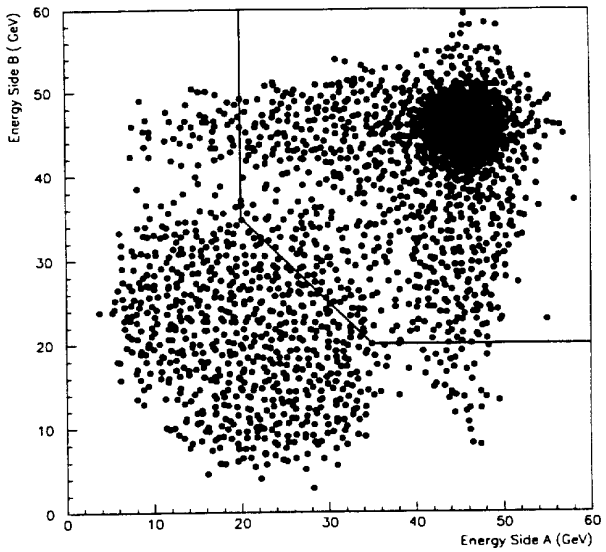

Figure 30: Largest reconstructed cluster energy on one side versus the largest reconstructed cluster energy on the other; the line indicates the cuts applied.

background due to random coincidence of off-momentum beam particles. The reconstructed energy for the largest cluster of one side is plotted versus that of the other in Figure 30. The energy distribution for the sum of the two largest clusters, before and after cuts, is shown in Figure 31. Events in the high energy tail of the distribution are consistent with accidental coincidences of Bhabha events with off-momentum beam background.

3. Radial fiducial cuts are applied, requiring one cluster to be within a 'tight' acceptance, and the opposite to be within a 'loose' acceptance. The tight and loose sides are alternated for each event; this alternation ensures that the acceptance is independent to first order of the interaction point position, both along and transverse to the beam direction [14]. The luminosity selection requires the tight-side cluster to lie within radial pads 4 to 12 (inclusive), while the loose-side cluster in the other calorimeter is accepted if it is within radial pads 2 to 15 (inclusive). To determine whether a cluster is inside the fiducial region, the 'radial energy asymmetry' is required to be positive; it is defined as

$$A_r = \frac{E_{in} - E_{out}}{E_{in} + E_{out}} , \tag{12}$$

where E_{in} is the energy inside a radial pad-row within the fiducial region and E_{out} is the energy in the radial pad-row outside.

4. An acoplanarity cut is applied based upon the azimuthal angular difference $\Delta\phi$ of the two largest clusters, $150° < \Delta\phi < 210°$. The $\Delta\phi$ distributions for real and Monte Carlo data (no background) are shown in Figure 32. The sources of excess events seen in the data outside the Bhabha peak are discussed in the next section.

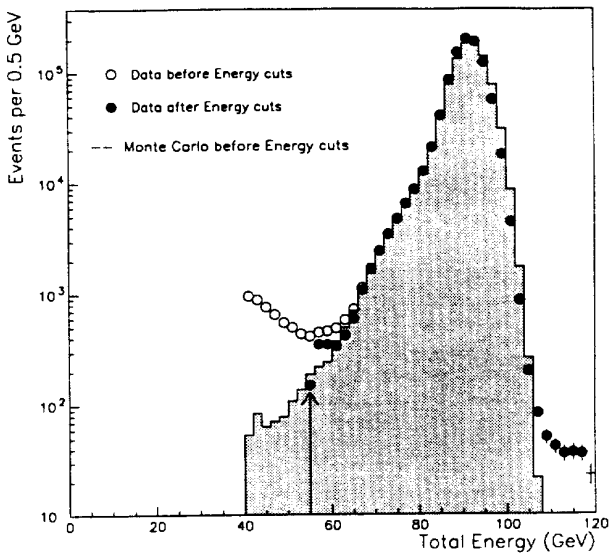

Figure 31: Energy distribution for the sum of the two largest clusters, shown as points for data before (open) and after (solid) energy cuts; the Monte Carlo simulation is shown as a histogram and the total energy cut indicated by the arrow.

11.2 Background rejection

Backgrounds to the Bhabha cross-section measurement come from two sources: accidental coincidences of off-momentum beam particles, and 'physics' processes which give events with electromagnetic clusters which pass the luminosity selection. The treatment of the data sample has been performed differently for the two: the beam related backgrounds, which are fill-dependent, are subtracted from the data, whereas the physics background has been treated as a cross-section correction.

Off-momentum particles in the LEP beam, spilling out, occasionally satisfy the coincidence trigger and pass the luminosity cuts. A single-arm trigger with a very low threshold of 9 GeV (typically) is used to estimate the rate at which this happens by measuring the rate and distribution of beam-related background in both calorimeters. During 1992, the background rate was found to be lower than the Bhabha rate by a factor of 7.0×10^{-4}; this factor was much lower in 1993. The artificial events built from single-arm triggers which lie in the same region may be compared with the observed events, and the shape of the prediction agrees well with that observed.

Four different sources of physics background sources have been considered; their contamination of the selected Bhabha sample has been estimated either with the help of Monte Carlo generators or by direct analytical calculations. The t-channel production of two (or three) hard photons [15] is the only non-negligible source of physics background. The total cross-section for the selected events corresponds to a 0.015 % contamination, and is added to the reference Bhabha cross-section.

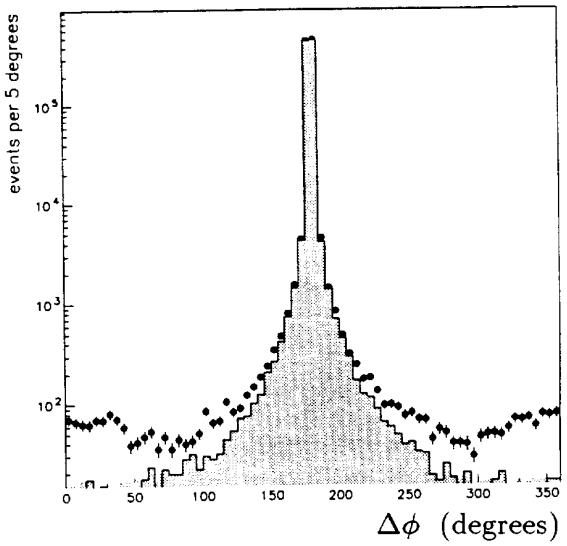

Figure 32: Distribution of the ϕ-difference $\Delta\phi$ between the 'tight-side' and 'loose-side' clusters. Data are plotted as points and the Monte Carlo simulation is shown as a histogram.

11.3 Luminosity measurement performance

The first check of the coincidence trigger uses events which satisfy the single-arm high threshold trigger on one side and which have energy deposits in both calorimeters. The coincidence trigger frequency for such events versus the energy in the opposite side measures the efficiency: it turns on at 12 GeV (the low threshold) and is fully efficient by 20 GeV. A second check uses selected Bhabha events and the independent triggers derived from different sets of planes to verify the efficiency of the coincidence trigger. The Bhabha coincidence trigger derived from the odd planes on one side and the even planes on the other, for example, is used to check the efficiency of the same trigger derived from the even planes on the first side and the odd planes on the other. The inefficiencies of sub-triggers are all well under 10^{-4}.

Showers are identified in each calorimeter by the reconstruction program using the energy deposited in each hit pad, corrected for the energy calibration. A simple and robust clustering algorithm has been developed to reliably locate electromagnetic showers without, however, separating a possible nearby cluster from a radiated photon. The low value of the minimum energy (30 MeV) required to connect pads in a cluster ensures that an electron/positron shower and a possible radiated photon shower are merged into the same cluster if they are separated by less than about 16 mrad. The total number of pads per cluster for clusters of about 45 GeV falls smoothly with radius from 91 pads at the inner fiducial cut to 82 pads at the outer cut, due essentially to the increasing pad-size with radius. The cluster is cut outside the fiducial region by the edge of the detector. Each cluster is characterized by its total energy and its barycenter position (r, ϕ and z). Radial and ϕ periodic corrections are applied to account for biases due to the barycenter method [13], and an additional radial correction is included to take into account pad curvature and edge effects.

The stability of the pedestals is continuously monitored during the data taking, leading

to a fill-to-fill drift of less than 2 MeV. The pad-to-pad energy calibration is obtained by measuring the response of each amplifier channel; this is achieved by pulsing individual channels (simultaneously for all the amplifiers). Both gain and inter-channel crosstalk are measured. A fitting procedure is applied giving net residuals below 0.7 %. Applying the gains obtained from the electronic calibration improves the resolution for fully contained 45 GeV showers from 6.2 % to 5.5 %, with a uniform energy response over the detector in r and ϕ. Taking into account detector effects not seen by the calibration procedure a final energy resolution of 4.9 % is achieved.

The spatial resolution on the barycenter position is not of prime importance in the performance as the radial cut does not rely on it, and the acoplanarity cut is wide enough to accept a modest resolution in ϕ. The average resolution on the radial barycenter position is about 150 μm and the azimuthal resolution varies from 0.2° at the outer radius to 0.3° at the inner radius. The radial resolution on the fiducial cut is 12 μm.

The accepted Bhabha cross-section is determined using the BHLUMI generator [16]. It must be corrected for the t-channel two hard-photon background (+0.015 %), and the missing Z-exchange contributions (+0.061 %), as evaluated from other generators [17]. The integrated luminosity is given by N_{Bhabha}/σ_{corr}, where N_{Bhabha} is the number of events passing the luminosity selection cuts, after background subtraction, and σ_{corr} is the corrected cross-section. The experimental precision in the 1992 luminosity measurement is estimated to be 0.09 %, shared between several sources including thermal expansion of the silicon-detector support ring, uncertainty in the value of the z separation of the calorimeters, and the fidelity of the Monte Carlo shower parametrization.

12 Conclusion

ALEPH is a detector designed for e^+e^- physics up to 200 GeV centre-of-mass energy. During the conception of ALEPH, emphasis was placed on high three-dimensional granularity and hermetic coverage for the tracking and calorimetry, on accurate vertexing, on good tracking via a large detector in 1.5 T magnetic field, and on precision luminosity determination. The resulting performance shows excellent multiparticle-detection and lepton-identification efficiency over 97 % of the solid angle. Hadron (π, K, p) identification was not emphasized but turns out to be adequate. These features have led to a detector for which the systematic errors are small in the measurements of physical quantities at LEP.

Acknowledgements

It is a pleasure to thank the technical personnel of the collaborating institutions for their support in constructing and maintaining the ALEPH experiment. Those of us from non-member states thank CERN for its hospitality.

References

[1] D. Decamp *et al.*, (ALEPH Collab.), Nucl. Instr. Meth. A **294** (1990) 121.

[2] G. Batignani *et al.*, 1991 IEEE Nuclear Science Symposium, Santa Fe, IEEE transactions on nuclear science, v.NS 39(4–5) (1992) Vol. 1, p. 438.

[3] G.J. Barber *et al.*, Nucl. Instr. Meth. A **279** (1989) 212.

[4] W.B. Atwood *et al.*, Nucl. Instr. Meth. A **306** (1991) 446.

[5] R. Frühwirth, HEPHY–PUB 503/87 (1987).

[6] D. Buskulic *et al.*, (ALEPH Collab.), Phys. Lett. B **313** (1993) 535.

[7] D. Buskulic *et al.*, (ALEPH Collab.), Phys. Lett. B **332** (1994) 209.

[8] A. Messineo *et al.*, Nucl. Instr. Meth. A **320** (1992) 177.

[9] E. Longo and I. Sestili, Nucl. Instr. Meth. A **128** (1987) 283.

[10] D. Buskulic *et al.*, (ALEPH Collab.), Nucl. Instr. Meth. A **346** (1994) 461.

[11] D. Decamp *et al.*, (ALEPH Collab.), Z. Phys. C **54** (1992) 211.

[12] D. Buskulic *et al.*, (ALEPH Collab.), 'Production of K^0 and Λ in hadronic Z decays', CERN–PPE/94–74, submitted to Z. Phys. C.

[13] D. Bédérède *et al.*, 'SICAL: a high precision silicon-tungsten luminosity calorimeter for ALEPH', to be published in Nucl. Instr. Meth. A.

[14] G. Barbiellini *et al.*, Atti Accad. Naz. Lincei **44** (1968) 233;
J.F. Crawford *et al.*, Nucl. Instr. Meth. A **127** (1975) 173.

[15] F.A. Berends and R. Kleiss, Nucl. Phys. B **186** (1981) 22.

[16] S. Jadach *et al.*, Phys. Lett. B **268** (1991) 253;
S. Jadach *et al.*, Comput. Phys. Commun. **70** (1992) 305;
S. Jadach and B.F.L. Ward, Phys. Rev. D **40** (1989) 3582.

[17] M. Böhm, A. Denner and W. Hollik, Nucl. Phys. B **304** (1988) 687;
F.A. Berends, R. Kleiss and W. Hollik, Nucl. Phys. B **304** (1988) 712.